Chemical Engineering Science 171 (2017) 576–598

Contents lists available at ScienceDirect

Chemical Engineering Science

journal homepage: www.elsevier.com/locate/ces

CFD modeling of a industrial-scale steam methane reforming furnace

Anh Tran [a], Andres Aguirre [a], Helen Durand [a], Marquis Crose [a], Panagiotis D. Christofides [a,b,*]

[a] Department of Chemical and Biomolecular Engineering, University of California, Los Angeles, CA 90095-1592, USA
[b] Department of Electrical Engineering, University of California, Los Angeles, CA 90095-1592, USA

HIGHLIGHTS

- Computational fluid dynamics modeling of the combustion chamber.
- Computational fluid dynamics modeling of the reforming tubes.
- Computational fluid dynamics modeling of steam methane reforming furnace.
- Model calibration and comparison with industrial plant data.

ARTICLE INFO

Article history:
Received 22 June 2016
Received in revised form 17 March 2017
Accepted 1 June 2017
Available online 9 June 2017

Keywords:
Process modeling
Process operation
Methane reforming
Industrial furnace
Computational fluid dynamics
Process engineering

ABSTRACT

Hydrogen is a required key material for petroleum refineries that convert crude oil into products with higher economic value and is often produced by the steam methane reforming (SMR) process, which synthesizes hydrogen and carbon oxides from methane and superheated steam in the presence of a nickel-based catalyst network in a steam methane reformer. To investigate methods for improving profits for a reformer while avoiding costly on-site parametric studies, a high-fidelity model of a steam methane reformer can be investigated. Motivated by this, the present work focuses on developing a computational fluid dynamics (CFD) model of an industrial-scale steam methane reformer that consists of 336 reforming reactors, 96 burners and 8 flue gas tunnels. The motivation for choosing the modeling strategies used in the industrial-scale steam methane reformer CFD model is discussed and is based on expected transport phenomena and chemical reactions within the reformer. Specifically, the finite rate/eddy dissipation turbulence-chemistry interaction model, global kinetic models of hydrogen/methane combustion, global kinetic model of the SMR process and standard $k-\epsilon$ turbulence model with the ANSYS Fluent enhanced wall treatment function are used to simulate the formation and consumption rates of all chemical components of the system. In addition, an empirical correlation for estimating the radiative properties of a homogeneous gas mixture, Kirchhoff's law, Lambert Beer's law and the discrete ordinate method are employed to simulate radiative heat transfer in the furnace side of an industrial-scale steam methane reformer. Moreover, the modeling strategies of the reforming tubes developed in our previous work are adopted to model 336 reforming tubes in the reformer. Subsequently, the boundary conditions (i.e., the reforming tube feed, burner feed and the energy leakage through the combustion chamber refractory wall) of the industrial-scale reformer CFD model are derived based on typical plant data. The simulation results produced by the industrial-scale reformer CFD model are shown to be in agreement with typical plant data reported in the SMR literature, with the simulation data generated by an industrial-scale reforming tube CFD model and with the simulation data generated by a reforming Gibbs reactor model, which validates the chosen modeling strategies and allows the CFD data to be considered to represent actual plant data with sufficient accuracy for use in industrial operating parameter studies.

1. Introduction

Hydrogen is one of the most important raw materials for petroleum refineries that convert crude oil into a variety of products with higher economic value (e.g., gasoline, jet fuel and diesel). Its unavailability can halt the production of these petroleum products

* Corresponding author at: Department of Chemical and Biomolecular Engineering, University of California, Los Angeles, CA 90095-1592, USA.
E-mail address: pdc@seas.ucla.edu (P.D. Christofides).

http://dx.doi.org/10.1016/j.ces.2017.06.001
0009-2509/

because hydrogen is the required reactant of the hydrotreating and hydrocracking processes (Kroschwitz and Howe-Grant, 1999). The demand for hydrogen by petroleum refineries has increased due to environmental restrictions and efforts to process heavier components of crude oil. In particular, the environmental requirement for low-sulfur-content fuels results in an increasing amount of hydrogen required in hydrotreating processes, and the attempt to process heavier components of crude oil known as bottom-of-the-barrel processing also increases the demand for hydrogen in hydrocracking processes (Udengaard, 2004; Zamaniyan et al., 2010). Additionally, hydrogen is an efficient energy carrier and can be used as a fuel.

A key method for hydrogen production in industry is the steam methane reforming (SMR) process (Amirshaghaghi et al., 2010; Ewan and Allen, 2005). The SMR process is an overall endothermic process in which raw natural gas (e.g., methane) reacts with high-pressure and high-temperature steam (superheated steam) in the presence of a nickel-based catalyst to produce hydrogen, carbon dioxide and carbon monoxide (Kroschwitz and Howe-Grant, 1999). The SMR process accounts for a significant proportion of the hydrogen that is produced worldwide (Ewan and Allen, 2005; Sadooghi and Rauch, 2013; Lipman, 2011).

A steam methane reformer (it will be referred to as "reformer" in the following text) is the core unit in the SMR process. Reformers come in four typical configurations (i.e., top-fired, side-fired, bottom-fired and terrace wall-fired reformers), and the locations of the burners govern the temperature distribution inside the reformers and the heat flux profiles along the tubular reforming reactors (they will be referred to as "reforming tubes" in the following text). In the SMR process, the designs that enable a high amount of heat transfer to the reforming tubes near the reforming tube inlets are favorable because of the endothermic and reversible nature of the process, and therefore, the present work focuses on the top-fired reformers that are typically used in hydrogen manufacturing plants.

The top-fired reformer is composed of two closed but not thermally isolated domains: a tube side, which consists of hundreds of reforming tubes, and a furnace side, which is a combustion chamber. The combustion chamber, which is insulated by refractory walls, is designed to contain the thermal energy released from the combustion of the furnace-side fuel to prevent this energy from dissipating to the surrounding air. Typically, only ~2–5% of the total fired duty is lost (Latham, 2008), while a significant percentage of the thermal energy (e.g., ~50%) is transferred to the reforming tubes, primarily by thermal radiation (de Lasa et al., 1992). The remaining energy exits the reformer at the chamber outlet by species transport. On the tube side, raw natural gas undergoes hydrotreating and hydro-desulfurization processes such that the major component of the pre-treated natural gas is methane. Subsequently, the pre-treated natural gas is mixed with superheated steam, and the mixture of reactants is fed into the reforming tubes in which the overall endothermic SMR process, driven by the thermal energy absorbed from the furnace side and facilitated by the nickel-based catalyst network, converts steam and methane into hydrogen and byproducts (i.e., carbon oxides).

In 2004, the hydrogen production rate and annual growth rate of hydrogen production in North America were estimated to be 6,700,000 Nm^3/h and above 4%, respectively, and the largest plant could produce up to 300,000 Nm^3/h (Latham, 2008). For instance, a hydrogen plant with a production rate of 112,000 Nm^3/h can spend up to 62 million dollars to purchase raw natural gas annually. Therefore, a small improvement in process efficiency can result in a great gain in profit margin for a plant. This became the driving force for the development of reformer study, and specifically, reformer parametric study has become a highly researched topic. Since the mid-1900s, extensive work has been conducted on the development of reformer first-principles modeling, and in the 1960s (McGreavy and Newmann, 1969), the first mathematical model of a complete reformer was developed. The mathematical models of reformers gradually became more sophisticated and highly complex in order to account for physical (i.e., the transport of momentum, material and energy) and chemical (i.e., combustion processes and the SMR process) phenomena taking place inside the unit. As a result, the mathematical model of the complete reformer is defined by two sets of highly non-linear coupled partial integro-differential equations with seven independent variables including the three spatial coordinates, the temporal variable, the wave number of electro-magnetic waves and its corresponding two angular coordinates (Mishra and Prasad, 1998). Therefore, characterizing the reformer by numerically determining the solution of the mathematical model of the complete reformer is a formidable task. In the effort to characterize reformers, previous studies of reformer modeling simplify the reformer mathematical model by avoiding simulating the combustion phenomena, and assume a profile for the energy released in the reaction zone due to the furnace-side oxidation (Latham, 2008; Latham et al., 2011; Zamaniyan et al., 2008) or a profile for the outer reforming tube wall temperature (Pantoleontos et al., 2012; Pedernera et al., 2003). Specifically, these assumptions substantially reduce the workload of the numerical solver. However, these profiles are often developed by extrapolating the scarcely available experimental data of bench-scale or pilot-scale versions of the system and, therefore, cannot be assumed to accurately represent the profiles that would be observed in an on-line reformer.

With improvements in technological performance, computational fluid dynamics (CFD) modeling became a powerful tool for predicting fluid behavior with a high level of accuracy. Specifically, CFD modeling can capture all geometry characteristics of systems of interest through computer-aided design software, which in turn allows CFD models to generate simulation results that can be expected to serve as reasonable substitutes for experimental data (Zhang et al., 2015). Therefore, it is reasonable to assume that simulation results generated by a well-designed reformer CFD model, which simulates typical transport and chemical phenomena observed in reformers while accurately accounting for the reformer geometry, are expected to be consistent with experimental data collected from industrial-scale plants. Furthermore, a well-designed CFD model of a reformer can provide insights into the system which cannot be captured in experimental data recorded from an on-site parametric study.

Motivated by the above considerations, we employ ANSYS Fluent CFD software to develop an industrial-scale reformer CFD model (for brevity, the CFD model is referred to as the "reformer CFD model") that is composed of 336 reforming tubes, 96 burners and 8 flue gas tunnels (details given in Section 2). Initially, we discuss the modeling methodology for the reformer CFD model including kinetic models of methane/hydrogen combustion phenomena, radiative heat transfer modeling, global kinetic model of the SMR process, turbulence-chemistry interaction modeling and thermodynamic modeling. The selection of appropriate models to simulate all essential transport phenomena and chemical reactions of the reformer with an affordable computational cost and reasonable computing time is based on expected transport and chemical reaction phenomena typically observed in the reformer. Specifically, the standard $k-\epsilon$ turbulence model with the ANSYS Fluent enhanced wall treatment function, finite rate/eddy dissipation (FR/ED) turbulence-chemistry interaction model and global kinetic models of combustion (Bane et al., 2010; Nicol, 1995) are integrated to simulate the non-premixed combustion characteristics (details given in Section 4.1). Additionally, an empirical correlation between the furnace-side radiative properties and temperature (Maximov, 2012), Kirchhoff's law, Lambert Beer's law and the

discrete ordinate method (ANSYS Inc., 2013) are adopted to simulate and quantify the rates of radiative heat transfer within the furnace-side mixture and between the furnace-side mixture and solid surfaces inside the reformer (i.e., combustion chamber refractory walls and outer reforming tube walls) (details given in Section 4.2). Furthermore, the reformer CFD model adopts the reforming tube modeling strategies developed in our previous work (Lao et al., 2016); specifically, the reforming tubes are modeled by the pseudo-homogeneous reactor model, the reforming tube walls are modeled by the ANSYS Fluent thin wall model, the catalyst network is modeled by the continuum approach and its effects on the tube-side flow are modeled by the ANSYS Fluent porous zone function. In the reforming tubes, the standard $k-\epsilon$ turbulence model with the ANSYS Fluent enhanced wall treatment function, global heterogeneous catalysis kinetic model of the SMR process (Xu and Froment, 1989) and FR/ED model are implemented to simulate the formation and consumption rates of the tube-side species in the turbulent reacting flow (details given in Section 5.1). The boundary conditions for the reforming tube inlet (referred to in the following text as "tube-side feed"), burner inlet (referred to in the following text as "furnace-side feed"), and combustion chamber refractory walls are derived from typical plant data (Latham, 2008). Finally, the simulation results generated by the reformer CFD model are rigorously validated by comparing them with the available data in the literature, converged solution produced by a single reforming tube CFD model and simulation results generated by a reforming Gibbs reactor of a commercial steady-state process simulator.

2. Industrial-scale steam methane reformer geometry

The reformer investigated in this work is developed based on an industrial-scale top-fired, co-current reformer designed by Selas Fluid Processing Corporation (Fig. 1). The reformer is approximately 16 m wide, 16 m long and 13 m tall. The reformer contains seven rows of forty-eight reforming tubes of which the external diameter, internal diameter and exposed length are 14.6 cm, 12.6 cm and 12.5 m, respectively. Inside these reforming tubes, commercial nickel-based catalyst pellets (i.e., alpha-alumina-supported nickel oxide denoted as NiO-αAl_2O_3) are used as packing material. At the combustion chamber ceiling, these rows of reforming tubes are separated by eight rows of twelve burners which are fed with a furnace-side feed composed of a fuel stream containing methane, hydrogen and carbon monoxide, and an oxidizer stream containing combustion air (Ar, N_2 and O_2). The rows of burners which are adjacent to the combustion chamber refractory walls and a single row of reforming tubes (for brevity these burners are denoted as "outer-lane burners"), are fed with a lower furnace-side feed flow rate than the rows of burners which are adjacent to two rows of reforming tubes (for brevity, these burners are denoted as "inner-lane burners"). Specifically, the furnace-side feed flow rate of the outer-lane burners is 60% of that of the inner-lane burners to avoid causing "over-firing" in the outer lanes and "under-firing" in the inner lanes, which would occur if the total furnace-side feed flow rate were evenly distributed to all burners. At the reformer floor, the rows of reforming tubes are separated by the rectangular intrusions known as flue gas tunnels or coffin boxes which extend from the front to the back of the combustion chamber along the rows of reforming tubes with a height of 3 m from the floor. Additionally, there are thirty-five extraction ports evenly distributed in a row along each side of the flue gas tunnels that allow the furnace-side mixture to enter the flue gas tunnels, and then to exit the combustion chamber through the front openings of the flue gas tunnels. In this work, we will focus on the development of a CFD model of the reformer described above.

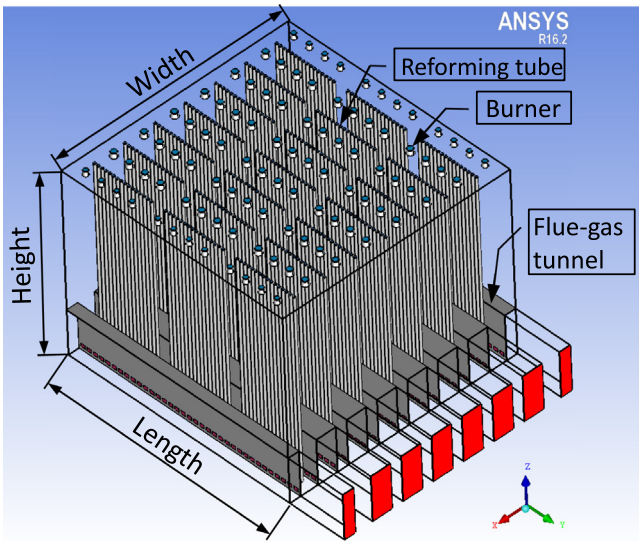

Fig. 1. The isometric view of an industrial-scale, top-fired, co-current reformer with 336 reforming tubes, which are symbolized by 336 smaller circles, 96 burners, which are denoted by 96 larger circles, and 8 flue gas tunnels, which are represented by 8 rectangular intrusions. The outer-lane burners are burners on the right and left boundaries of the figure, while the inner-lane burners are slightly larger than the outer-lane burners in the figure.

3. Industrial-scale steam methane reformer mesh

In the CFD study of the reformer, the reformer volume is divided into small and discrete subdomains also known as grids (a collection of grids is referred to as a mesh), within which spatial variations are, though not negligible, significantly less drastic than those in the overall domain. Then, the reformer mathematical model (i.e., two sets of highly non-linear coupled integro-differential equations with seven independent variables) is discretized and numerically solved within each grid to characterize the fluid-flow and temperature fields. Then, the numerical solutions of the grids are patched together to reconstruct the solution of the original domain. Hence, creating a mesh with acceptable mesh quality is a critical task that determines the success level of CFD modeling because a CFD model built from a poor quality mesh has a slow speed of convergence (Batdorf et al., 1997) and is more likely to converge to an inaccurate solution as mesh quality directly determines solver discretization error (ANSYS Inc., 2013).

There are two major classes of meshing strategies in ANSYS ICEM, i.e., the unstructured tetrahedral meshing strategy (for simplicity, it is denoted as "unstructured meshing") and the multi-block structured hexahedral meshing strategy (for simplicity, it is denoted as "structured meshing"). The unstructured meshing procedure creates a collection of predominantly tetrahedral grids that are arranged in an irregular pattern, while the structured meshing procedure creates a collection of hexahedral grids that are arranged in a pattern specified by the user of the mesh creation software. Although unstructured meshing is generally more proficient at approximating complicated geometries than structured meshing, the ANSYS ICEM environment offers an O-grid Block function that can be utilized to enhance the ability of structured meshing to approximate curvy geometry characteristics by re-arranging existing grid lines into an *O* shape to effectively improve the overall hexahedral mesh quality. In the creation of the reformer hexahedral mesh in this work, the O-grid Block function can be used for meshing of the burner geometries, which have a frustum-like structure, and the reforming tubes, which have a cylindrical structure. As shown in Fig. 2(a)–(c), the structured

meshing procedure with the O-grid Block function can capture the geometries of the reformer components (e.g., the inner-lane burners, outer-lane burners and reforming tubes) that cannot be represented with straight lines. Therefore, because we can capture all aspects of the reformer geometry with the structured meshing technique, and because for wall-bounded systems like the reforming tubes, a CFD model built from structured meshing generally generates a converged solution closer to experimental data and also is expected to have a superior speed of convergence compared to other CFD models built from unstructured meshing when the system is decomposed into the same number of discrete grids (ANSYS Inc., 2013; Lao et al., 2016; Duan et al., 2015), the reformer mesh is created using structured meshing in this work. The good agreement of our CFD results (presented in Section 9) with typical plant data (compared in Section 10) utilizing this meshing strategy shows that the meshing method employed was adequate for obtaining results that are consistent with typical plant data.

In the reformer mesh, the grids are not uniformly distributed, but are more dense in regions expected to have large momentum, material, and temperature gradients, such as in the neighborhood of the reforming tube walls (where heat transfer from the furnace-side to the tube-side is expected to create temperature gradients that must be captured through a denser mesh as shown in Fig. 3) and in the regions directly under the burners that correspond to the flames (where the mixing-limited nature of non-premixed combustion is expected to create species and flow characteristics that should be captured with a denser mesh as shown in Fig. 4). This design of the reformer mesh aims to reduce the stiffness of the spatial gradients of the transport variables, which allows the ANSYS Fluent CFD solver to obtain the numerical solution of the reformer CFD model with a shorter computing time.

In CFD, the reformer mesh must be discretized into a sufficient number of grids so that the CFD simulation data becomes mesh-independent. Our studies with three different mesh sizes of approximately 13, 29 and 41 million cells indicated that a mesh size of about 29 million cells produces mesh-independent results. Specifically, the reformer mesh contains 29,099,252 hexahedral grids, 88,798,168 quadrilateral faces and 30,584,930 nodes. The quality of the resulting mesh is evaluated utilizing the three mesh quality evaluation criteria (the minimum orthogonal factor, maximum ortho skew and aspect ratio) suggested by the manufacturer ANSYS Inc. of the commercial CFD software package utilized to develop the reformer CFD model in this work (other potential mesh evaluation criteria not specified by ANSYS Inc. were not utilized because ANSYS Inc. did not indicate recommended ranges for such properties that would suggest appropriate mesh quality based on such other criteria). ANSYS Inc. suggests that if the values of the three

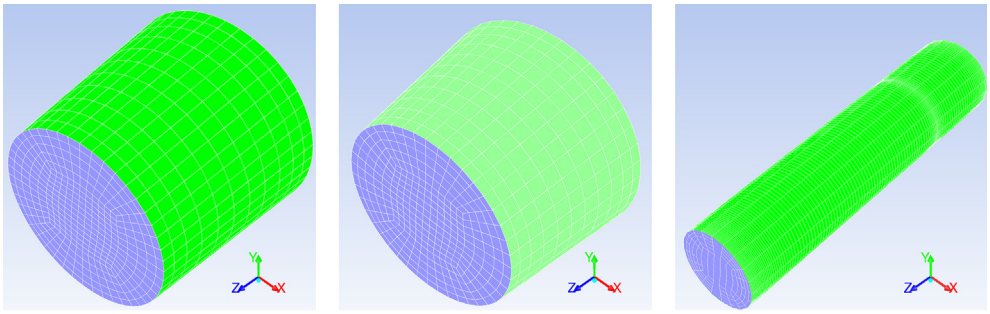

Fig. 2. Isometric view of the hexahedral structured mesh of the outer-lane burner (a), inner-lane burner (b) and reforming tube (c). This figure demonstrates that the meshes of both the inner-lane and outer-lane burners, as well as the mesh of the reforming tubes, created by the O-grid Block function of ANSYS ICEM have the exact geometries of the corresponding components. In Fig. 2(c), the radial direction of the reforming tube is scaled up by 20 times for display purposes.

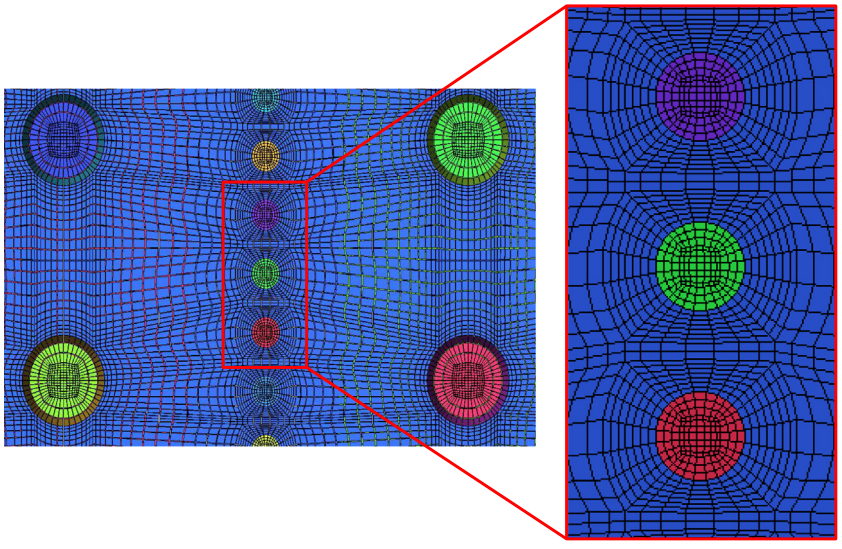

Fig. 3. A sample of the top view of the hexahedral structured mesh of the reformer, where a row of reforming tubes is adjacent to two inner-lane burners. In Fig. 3, the reforming tube inlets and burner inlets are assigned with different color for display purposes.

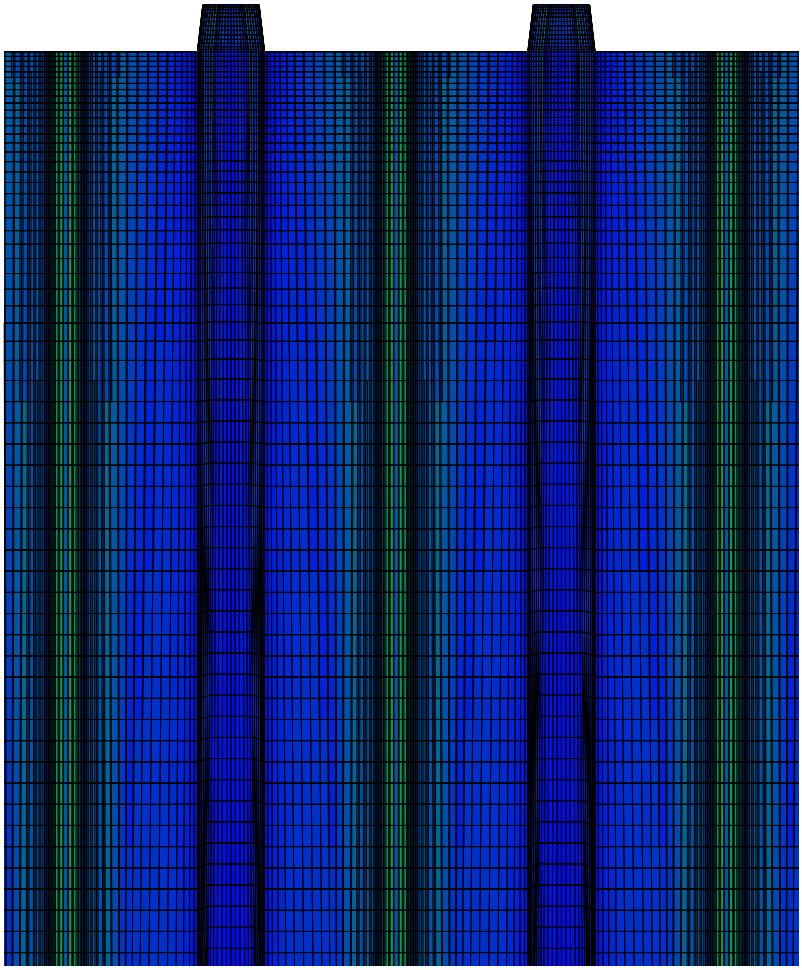

Fig. 4. A sample of the vertical cross section of the hexahedral structured mesh of the reformer.

Table 1
Mesh quality of the reformer mesh.

	The reformer mesh	Recommended range
Minimum orthogonal factor	0.181	0.167–1.000
Maximum ortho skew	0.819	0.000–0.850
Maximum aspect ratio	28.5	1.000–100.0

suggested criteria for all subdomains (i.e., mesh quality) are within the recommended ranges shown in Table 1, the mesh can be considered to have reasonably good quality and can be used to generate CFD results (regardless of whether some subdomains have values close to the boundary of the recommended range, which would cause the values in Table 1 to be closer to the limits of the recommended ranges since the ANSYS Inc. criteria are for the worst-case values among all subdomains). Because the values of the minimum orthogonal factor, maximum ortho skew, and maximum aspect ratio among all subdomains are within the ranges recommended by ANSYS Inc., the mesh of the industrial-scale reformer is considered to have reasonably good quality (this is further validated by the good agreement of the CFD data generated using this mesh and typical plant data as discussed in Section 10). Although the minimum orthogonal factor and maximum ortho skew of the reformer mesh are close to the lower limits as shown in Table 1, the average orthogonal factor (0.965) and average ortho skew (0.035) of the reformer mesh are close to the ideal values of 1.000 and 0.000, respectively. Hence, we use the reformer mesh with approximately 29 million cells to create the reformer CFD model.

4. Furnace chamber modeling

4.1. Combustion reaction kinetic model and turbulence-chemistry model

In the combustion chamber, reducing agents in the furnace-side feed are oxidized to their highest oxidation states generating carbon dioxide, water and a large amount of thermal energy, which is used to drive the SMR process inside the reforming tubes. The chemistry of the combustion phenomena is a complex network of sequential elementary reactions governed by the concentrations of free radicals. For instance, the complete mechanism of the hydrogen combustion phenomena generating water involves more than 20 elementary reactions with various intermediates, and the corresponding detailed kinetic model consists of more than 20 distinct reaction rates (Turns, 1996). Although it is possible to implement such a detailed kinetic model in the reformer CFD model, the CFD model would be no longer meaningful for industrial applications as it would take a long computing time to generate the CFD simulation data. As a result, global kinetic models for the combustion of methane (Nicol, 1995) and hydrogen (Bane et al., 2010) are adopted to reduce the computational requirement for simulating the reformer CFD model to model the combustion of the furnace-side feed:

Global kinetic model of methane combustion:

$$CH_4(g) + 1.5O_2(g) \xrightarrow{R_1} CO(g) + 2H_2O(g), \quad (1a)$$

$$R_1 = 10^{15.22}[CH_4]^{1.46}[O_2]^{0.5217}\exp(-20643/T_{comb}) \quad (1b)$$

$$CO(g) + 0.5O_2(g) \underset{R_3}{\overset{R_2}{\rightleftharpoons}} CO_2(g) \quad (1c)$$

$$R_2 = 10^{14.902}[CO]^{1.6904}[O_2]^{1.57}\exp(-11613/T_{comb}) \quad (1d)$$

$$R_3 = 10^{14.349}[CO_2]\exp(-62281/T_{comb}) \quad (1e)$$

Global kinetic model of hydrogen combustion:

$$H_2(g) + 0.5O_2(g) \xrightarrow{R_4} H_2O(g) \quad (2a)$$

$$R_4 = 4.61 \times 10^{15}[H_2][O_2]\exp(-10080/T_{comb}) \quad (2b)$$

where R_1, R_2, R_3 and R_4 (kmol m^{-3} s^{-1}) are the intrinsic volumetric reaction rates, T_{comb} (K) and $[i]$, $i = CO_2$, CO, CH_4, H_2, O_2 (kmol m^{-3}) are the temperature and species molar concentrations of the furnace-side mixture. It is worth noting that because the empirical kinetic formulas (Eqs. (1) and (2)) are in the Arrhenius form, they can be directly integrated into the reformer CFD model to simulate the formation and consumption rates of the furnace-side species.

In the reformer, the furnace-side feed composed of two separate streams, i.e., the fuel stream and the oxidizer stream, is combusted inside the combustion chamber to generate the required fired duty for the SMR process. The intrinsic nature of non-premixed combustion is turbulent mixing-controlled, i.e., the rate of the chemical reactions is relatively faster than that of mixing on which the observed reaction rates of furnace-side species depend. In the remainder of this section, we demonstrate a modeling strategy that allows the reformer CFD model to simulate the behavior of non-premixed combustion processes of the furnace-side feed.

Specifically, in the reformer CFD model, the fuel stream and air stream of the furnace-side feed are assumed to be well-mixed as shown in Table 2 prior to being fed into the combustion chamber, and the combustion phenomena of methane and hydrogen are modeled by the premixed combustion model. However, the intrinsic nature of non-premixed combustion phenomena must be shown in the simulation results generated by the reformer CFD model. This issue is resolved by using the finite-rate/eddy-dissipation (FR/ED) model as the turbulence-chemistry interaction model to simulate the reaction rates of the furnace-side species. In particular, the FR/ED model utilizes the global kinetic models of methane/hydrogen combustion phenomena (shown in Eqs. (1) and (2)), finite rate formula (shown in Eq. (3c)) and eddy-dissipation rates (shown in Eqs. (3a) and (3b)) to estimate the observed reaction rates of the furnace-side species (ANSYS Inc., 2013). The formulation of the FR/ED model is presented as follows:

Table 2
Furnace-side inlet operating conditions of the inner-lane burner in which $x^i_{comb,inlet}$ represents the mole fraction of species i in the furnace-side feed.

Pressure (kPa)	131.3
Temperature (K)	532.9
Flow rate (kg/s)	1.1358
$x^{H_2O}_{comb,inlet}$	0.0039
$x^{O_2}_{comb,inlet}$	0.1610
$x^{Ar}_{comb,inlet}$	0.0071
$x^{N_2}_{comb,inlet}$	0.6008
$x^{H_2}_{comb,inlet}$	0.0592
$x^{CO_2}_{comb,inlet}$	0.0972
$x^{CO}_{comb,inlet}$	0.0208
$x^{CH_4}_{comb,inlet}$	0.0501

$$R_{i,j} = \nu_{i,j} M_i A \rho_{comb} \frac{\epsilon_{comb}}{k_{comb}} \min_{\mathcal{R}} \left(\frac{Y_{\mathcal{R}}}{\nu_{\mathcal{R},j} M_{\mathcal{R}}} \right) \quad (3a)$$

$$R_{i,j} = \nu_{i,j} M_i AB \rho_{comb} \frac{\epsilon_{comb}}{k_{comb}} \frac{\sum_{\mathcal{P}} Y_{\mathcal{P}}}{\sum_{n}^{N} \nu_{n,j} M_n} \quad (3b)$$

$$R_{i,j} = \nu_{i,j} M_i R_j \quad (3c)$$

where $R_{i,j}$ (kg m^{-3} s^{-1}) and $\nu_{i,j}$ are the observed reaction rate and stoichiometric coefficient of species i in reaction j, M_i (kg kmol^{-1}) is the molecular weight of species i, $Y_{\mathcal{R}}$ and $M_{\mathcal{R}}$ are the mass fraction and molecular weight of a specified reactant $\mathcal{R}$, $\nu_{\mathcal{R},j}$ is the stoichiometric coefficient of a specified reactant $\mathcal{R}$ in reaction j, $A = 4.0$ and $B = 0.5$ are the default empirical constants of the FR/ED model (Magnussen and Hjertager, 1977), k_{comb} (m^2 s^{-2}) and ϵ_{comb} (m^2 s^{-3}) are the turbulence kinetic energy and dissipation rate (which will be discussed in Section 7), $Y_{\mathcal{P}}$ is the mass fraction of a product species $\mathcal{P}$ in reaction j, R_j (kmol m^{-3} s^{-1}) is the intrinsic volumetric reaction rate of reaction j from Eqs. (1) and (2), ρ_{comb} (kg m^{-3}) is the density of the furnace-side mixture, n is the index of the product species involved in reaction j and N represents the number of chemical species in reaction j (ANSYS Inc., 2013). When the FR/ED model is integrated in the reformer CFD model, the reaction rate of each furnace-side species is calculated based on the three different methods presented in Eqs. (3a), (3b) and (3c) for which the smallest estimate corresponding to the slowest rate is set as the observed rate (Luan et al., 2013). In other words, in the reaction-limited zone, the observed reaction rates of the furnace-side species are computed by the finite rate formula (Eq. (3c)), whereas in the transport-limited zone, they are computed by the eddy-dissipation formulas (Eqs. (3a) and (3b)). Particularly, because the furnace-side temperature of 532.9 K at the inner-lane/outer-lane burner inlets is relatively low compared to the typical operating furnace-side temperature, the finite rate formula is expected to predict slower reaction rates of furnace-side species than those estimated by the eddy-dissipation formulas. This is because the activation temperature values of methane/hydrogen combustion phenomena derived from the chosen kinetic models (Eqs. (1) and (2)) are substantially larger than the furnace-side feed temperature, and the concentrations of reacting species are diluted by the presence of inert furnace-side species (i.e., nitrogen and argon), which account for ~61% of the furnace-side feed molar flow rate. Furthermore, the contour plots of furnace-side compositions and energy released from the combustion of the furnace-side feed (presented in Section 9) generated by the reformer CFD model indicate that the oxidation rates of methane and hydrogen detected in the vicinity of the inner-lane/outer-lane burner inlets are slow, which matches well with the expected observations. The results suggest that the reaction rates of furnace-side species estimated by the FR/ED model in these regions mimic the effect of initial mixing of fuel and oxidizer streams in non-premixed combustion phenomena. As the oxidation of the furnace-side feed gradually proceeds to produce combustion products (i.e., carbon dioxide and water), the enthalpy of reactions is released causing the temperature of the furnace-side mixture to increase, which allows the methane/hydrogen combustion phenomena to eventually overcome the activation energy barrier. Therefore, in the flame bodies, the finite rate formula is expected to yield higher estimates for the reaction rates of the furnace-side species than those based on the eddy-dissipation formulas. As a result, the premixed combustion model coupled with the FR/ED model allows the reformer CFD model to simulate the turbulent-mixing controlled characteristics of non-premixed methane/hydrogen combustion phenomena.

4.2. Radiative heat transfer modeling

In high-temperature applications such as the SMR process, the contribution of thermal radiation to the total heat transfer rate cannot be neglected. In Olivieri and Vegliò (2008), thermal radiation has also been reported as the dominant mode of heat transfer in a reformer as it accounts for about ~95% of the total heat transfer rate to the tube side. This is because the rates at which thermal energy is transferred by conduction and convection are known to be approximately proportional to the difference in temperature, while the rate of thermal energy transferred by radiation is proportional to the difference between the temperatures raised to the fourth power. Therefore, in the high-temperature combustion chamber of the reformer, thermal radiation would be expected to contribute significantly to heat transfer.

The study of radiative heat transfer is not often conducted experimentally for reformers because of the severe operating temperature of 2050 K inside the reformer and the absence of an accurate means to measure the radiative heat transfer rate. Additionally, the experimental data type related to the total heat transfer rate which can be collected from an on-line reformer may be the outer reforming tube wall temperature at designated locations (e.g., three along the heated tube length of 12.5 m) (Latham et al., 2011). This data is expected to carry a high degree of uncertainty because of the way by which the outer reforming tube wall temperature is measured, which involves a system of infrared (IR) cameras that gains access into the reformer to monitor the outer reforming tube wall temperature through peepholes in the combustion chamber refractory walls (Latham, 2008). Therefore, the study of radiative heat transfer in reformers has been conducted primarily by a modeling approach.

To model thermal radiation, it is essential that the role of radiating media in thermal radiation is well understood. Specifically, radiating media, which can consist of various particle types (e.g., neutral molecules, ionic molecules, free electrons and atoms), participate in thermal radiation by absorbing or emitting radiative energy in the form of electromagnetic waves for which the corresponding energy content denoted by E_{wave} can be evaluated as follows:

$$E_{wave} = h \cdot \nu_{wave} \tag{4}$$

where h is Plank's constant and ν_{wave} (s^{-1}) is the frequency of an electromagnetic wave. When a radiating particle absorbs/emits radiative energy, it absorbs/emits an electromagnetic wave, and its energy increases/decreases correspondingly by the amount of the electromagnetic wave. In air-fired reformers, radiating media (e.g., the furnace-side mixture) can be assumed to be neutral molecules, and thus, the furnace-side mixture can absorb an electromagnetic wave if the radiative energy content of the electromagnetic wave is equal to the transition energy required for the energy level to elevate to higher discrete bound states which correspond to the vibrational, rotational and electronic modes. Hence, radiative heat transfer in the furnace-side mixture is spectrum dependent because the furnace-side mixture only absorbs/emits radiative energy at certain frequencies in the entire spectrum. In the furnace-side mixture, monatomic molecules (e.g., argon) and diatomic molecules (e.g., oxygen, nitrogen, hydrogen and carbon monoxide) can be considered to be transparent to radiation (Maximov, 2012). As a result, the furnace-side mixture can be treated as a $H_2O - CO_2$ mixture in the sense that the radiative properties of the furnace-side mixture can be considered to depend only on those of H_2O and CO_2 (i.e., the furnace-side mixture must be modeled as a radiatively participating medium with radiative properties developed from those of H_2O and CO_2).

The combustion modeling literature suggests that the radiative properties of the furnace-side mixture can be estimated with the line-by-line model (LBLM), statistical narrow band model (SNBM) and exponential wide band model (EWBM); nevertheless, because of the excessively high required computational cost of utilizing these models for large-scale systems, they are not compatible with CFD models developed for industrially-oriented applications (Maximov, 2012). In the present work, a more computationally efficient empirical model developed in Maximov (2012), which is designed for air-fired combustion systems, is utilized. The empirical model uses the temperature, composition and total pressure of the furnace-side mixture and the characteristic dimension of the combustion chamber in the estimation of the total emissivity of the furnace-side mixture. The results reported in Maximov (2012) show that the total emissivity of an air-fired combustion system calculated from the empirical model is within ±5% of the data generated by the SNBM, and the computing time is decreased by a factor of at least ten. Hence, the following empirical model for the total emissivity of the furnace-side mixture is expected to offer a significant reduction in the computing time and to predict sufficiently accurate estimates of the furnace-side total emissivity:

$$a_i = a_{10,i} + a_{11,i} \cdot x_{comb}^{H_2O} + a_{12,i} \cdot x_{comb}^{CO_2} + a_{13,i} \cdot x_{comb}^{H_2O} \cdot x_{comb}^{CO_2} \tag{5a}$$

$$L = 3.6 \cdot \frac{V_{comb}}{A_{comb}} \tag{5b}$$

$$\begin{aligned} \epsilon_{rad} = \; & a_1 + a_2 \cdot \ln(T_{comb}) + a_3 \cdot \ln(P_{comb}^t L) + a_4 \cdot [\ln(T_{comb})]^2 \\ & + a_5 \cdot [\ln(P_{comb}^t L)]^2 + a_6 \cdot \ln(T_{comb}) \cdot \ln(P_{comb}^t L) \end{aligned} \tag{5c}$$

where $a_{j,i}$ and a_i are the model constants of the empirical model as shown in Table 3, $x_{comb}^{H_2O}$ and $x_{comb}^{CO_2}$ are the mole fractions of water and carbon dioxide in the furnace-side mixture, $V_{comb} \sim 3303.5\ m^3$, $A_{comb} \sim 5204.4\ m^2$ and $L \sim 2.3$ m are the volume, total surface area and characteristic dimension of the combustion chamber, respectively, and P_{comb}^t and ϵ_{rad} are the total pressure and total emissivity of the furnace-side mixture. The empirical model of the furnace-side total emissivity is designed for air-fired combustion systems, and as a result, the total pressure inside the furnace chamber in Maximov (2012) as well as in the present work is assumed to be constant and is taken to be near atmospheric pressure of 100 kPa (i.e., 1 bar).

Though the correlation of Eq. (5) depends on $x_{comb}^{CO_2}$ and $x_{comb}^{H_2O}$, which vary in the flame region of the furnace-side, the flame physical volume (i.e., the reaction zones of the combustion of the furnace-side feed) accounts for a small fraction of the total volume of the combustion chamber. Therefore, the region within which ϵ_{rad} would vary due to the changes in a_i, $i = 1, \ldots, 6$, would be expected to be small compared to the dimensions of the furnace-side within which radiation is occurring. Furthermore, the difference in the furnace-side composition between the combustion product and the furnace-side feed is small, which is due to the fact that the inert gases (i.e., nitrogen and argon) of the furnace-side feed account for ~61.0% of the total molar flow rate, while the fuel (i.e., methane and hydrogen) only accounts for ~11.0%. Specifically, the differences in the average mole fractions of H_2O and CO_2

Table 3
Empirical constants of the correlation of the furnace-side mixture total emissivity with temperature. These constants are used in the calculation of a_i (Eq. (5a)) (Maximov, 2012).

a_i	$a_{10,i}$	$a_{11,i}$	$a_{12,i}$	$a_{13,i}$
$i = 1$	−2.756	−12.091	−2.074	8.90
$i = 2$	1.0155	3.827	0.649	−2.48
$i = 3$	0.284	−1.024	0.421	−0.64
$i = 4$	−0.085	−0.286	−0.047	0.17
$i = 5$	0.0104	−0.067	−0.016	0.19
$i = 6$	−0.0272	0.162	−0.061	0.08

between the furnace-side feed and the combustion product change from 0.0039 to ~0.170 and from 0.0972 to ~0.175, respectively. As a result, the change in ϵ_{rad} between its value at the furnace-side inlet conditions and the complete oxidation condition of the furnace-side feed is not expected to be necessary to account for within the radiation calculations, especially given the small flame volume over which ϵ_{rad} varies. Therefore, to reduce computation time, $x_{comb}^{H_2O}$ and $x_{comb}^{CO_2}$ are both approximated as constants at 0.170 and 0.175, respectively, in calculating ϵ_{rad} according to Eq. (5). Moreover, the characteristic dimension L of the reformer, which is estimated by Eq. (5b) based on the volume and total enclosure surface area of the combustion chamber, is also a constant, as is P_{comb}^{t}. As a result, the furnace-side total emissivity reduces to a function only of the furnace-side temperature (it is noted that the approximation of a constant furnace-side composition in calculating ϵ_{rad} does not imply that other properties of the furnace-side mixture should be modeled to be independent of composition; modeling the composition of the furnace-side is important in capturing, for example, the observed reaction rates of the furnace-side species, which determines the heat release profile of the combustion of the furnace-side feed).

Next, the absorption coefficient of the furnace-side mixture is related to the value of ϵ_{rad} from the empirical model of Eq. (5) through Kirchhoff's law and Lambert Beer's Law as follows:

$$\sigma_a = -\frac{\ln(1-\epsilon_{rad})}{L} \tag{6}$$

where σ_a is the absorption coefficient of the furnace-side mixture. It is important to note that the correlation of the absorption coefficient in Eq. (6) inherits all assumptions that are used to develop the correlation of the total emissivity, and therefore, it is also a function of only the furnace-side temperature. Subsequently, an absorption coefficient data set within the operating temperature range of the reformer is obtained by the correlations of Eqs. (5) and (6) and is fit with a second-order polynomial function by using a least-squares linear regression method. The result of this fit is

$$\sigma_a = 2.10\times10^{-8}\cdot T_{comb}^2 - 2.06\times10^{-4}\cdot T_{comb} + 0.456, \tag{7}$$

which will be utilized in the reformer CFD model.

The next step in modeling radiation within the furnace side is choosing a suitable radiation model.The present work is facilitated by the ANSYS Fluent CFD solver, which only supports a limited number of thermal radiation models. Specifically, ANSYS Fluent uses one of five radiative heat transfer models (i.e., Rosseland, $P-1$, discrete transfer radiation model (DTRM), surface to surface (S2S) model and discrete ordinate model (DOM)) to estimate the energy transferred by thermal radiation in high-temperature applications in which thermal radiation cannot be ignored. Among the five radiative heat transfer models, the DOM is the most versatile model (ANSYS Inc., 2013). In particular, the DOM can estimate heat transfer by radiation within absorbing, emitting and scattering media and between the participating media and opaque/semi-transparent walls. In addition, unlike the Rosseland and $P-1$ approximation which are only applicable for high optical thickness systems, the DOM can be used in any high-temperature application including the reformer in which the optical thickness is not well-defined because of the complex reformer interior. Unlike the S2S model which ignores the presence of the participating media, the DOM can account for the effect of the absorbing and emitting furnace-side mixture. Additionally, unlike the DTRM which uses the ray tracing technique and is more prone to error due to ray effects, the DOM converts the partial integro-differential radiative transfer equation (RTE) with seven independent variables into a finite number of transport equations of radiation intensity, which depends on the solid angle discretization parameters of the DOM.

Table 4
Properties of the combustion chamber refractory walls.

Density ($kg\,m^{-3}$)	3950
Heat capacity ($J\,kg^{-1}\,K^{-1}$)	718
Thermal conductivity ($W\,m^{-1}\,K^{-1}$)	2.6
Emissivity	0.65

In particular, by default in each octant space the azimuthal division is equal to two, and the polar division is equal to two, which allows the DOM to generate 32 partial differential equations of radiation intensity corresponding to 32 discrete direction vectors $\vec{s}$ specifying the directions at which energy is transferred by radiation. As a result, the radiative heat transfer rate obtained by solving the equations of radiation intensity is expected to require a relatively lower computational cost than is required to directly solve the RTE. In this work, radiative heat transfer between the furnace-side mixture, combustion chamber refractory walls and outer reforming tube walls will be quantified by the discrete ordinate method (DOM). The description of the DOM of an absorbing, emitting and non-scattering gray gas can be found in ANSYS Inc. (2013).

It is critical to a successful modeling task to realize that the internal emissivity of the wall surface is an intrinsic property of the surface, and therefore, it only depends on the surface's characteristics, e.g., the surface texture, instead of the surface material. In the reformer CFD model, the emissivity coefficients for the wall surfaces are assumed to be independent of the furnace-side temperature and are constant. Specifically, the emissivity coefficients of the reforming tubes, refractory wall and tunnel wall are chosen to be 0.85, 0.65 and 0.65, respectively, and additional physical properties of the refractory wall and tunnel wall are shown in Table 4 (Latham, 2008).

5. Reforming tube modeling

In the present work, the 336 reforming tubes are modeled by the pseudo-homogeneous reactor model, the reforming tube walls are modeled by the ANSYS Fluent thin wall model, the catalyst network is modeled by the continuum approach and its effects on the tube-side flow are modeled by the ANSYS Fluent porous zone function. These modeling strategies were utilized due to their success in generating CFD data with good agreement with typical plant data for a single reforming tube with an assumed outer reforming tube wall temperature profile (i.e., the furnace-side and its interactions through heat transfer with the tube-side were not simulated) in Lao et al. (2016). In the remainder of this section, the modeling strategies of the kinetic model of the SMR process and the catalyst network are presented.

5.1. Reforming reaction kinetic model

On the macroscopic scale, the SMR process consumes the thermal energy produced by the combustion of the furnace-side feed to convert steam and methane into hydrogen and carbon oxides in the presence of a nickel-based catalyst network, and the tube-side composition is reported to be close to the equilibrium composition at the reforming tube exit (Xu and Froment, 1989). On the microscopic scale, the reactants are transported from the bulk of the tube-side mixture to the surface of the catalyst network by convective mass transfer driven primarily by the reactant concentration gradients, which are generated by the external diffusion resistance of the catalyst network. Then, they diffuse down the second reactant concentration gradients from the surface of the catalyst network through the catalyst medium to the catalyst active

sites, where the SMR process occurs to generate the desired hydrogen along with carbon oxides. The reactant concentration gradients within the catalyst are generated by the internal diffusion resistance of the catalyst network. Finally, the products diffuse from the catalyst active sites back to the surface of the catalyst network, and eventually emerge back into the tube-side mixture. A kinetic model that provides a rate formula for each microscopic event of the SMR process is unsuitable for the reformer CFD simulation because it would be expected to require a significant computation time. Therefore, a global kinetic model of the SMR process proposed in Xu and Froment (1989), which is derived based on the Langmuir–Hinshelwood mechanism (i.e., the heterogeneous catalysis kinetic model) and is formulated in kg (kg of catalyst)$^{-1}$ s^{-1}, is utilized to lessen the computational demand without substantially sacrificing the accuracy of the simulation results:

$$CH_4(g) + H_2O(g) \rightleftarrows CO(g) + 3H_2(g),$$

$$R_5 = \frac{k_1}{\left(p_{tube}^{H_2}\right)^{2.5}}\left(p_{tube}^{CH_4}p_{tube}^{H_2O} - \frac{\left(p_{tube}^{H_2}\right)^3 p_{tube}^{CO}}{K_1}\right)/DEN^2 \tag{8a}$$

$$CO(g) + H_2O(g) \rightleftarrows CO_2(g) + H_2(g),$$

$$R_6 = \frac{k_2}{p_{tube}^{H_2}}\left(p_{tube}^{CO}p_{tube}^{H_2O} - \frac{p_{tube}^{H_2}p_{tube}^{CO_2}}{K_2}\right)/DEN^2 \tag{8b}$$

$$CH_4(g) + 2H_2O(g) \rightleftarrows CO_2(g) + 4H_2(g),$$

$$R_7 = \frac{k_3}{\left(p_{tube}^{H_2}\right)^{3.5}}\left(p_{tube}^{CH_4}\left(p_{tube}^{H_2O}\right)^2 - \frac{\left(p_{tube}^{H_2}\right)^4 p_{tube}^{CO_2}}{K_3}\right)/DEN^2 \tag{8c}$$

$$DEN = 1 + \frac{K_{H_2O}p_{tube}^{H_2O}}{p_{tube}^{H_2}} + K_{CO}p_{tube}^{CO} + K_{H_2}p_{tube}^{H_2} + K_{CH_4}p_{tube}^{CH_4} \tag{8d}$$

where K_{H_2}, K_{CH_4} and K_{CO} are adsorption constants for H_2, CH_4 and CO, K_{H_2O} is a dissociative adsorption constant of H_2O, K_1, K_2 and K_3 are equilibrium constants of the reactions in Eqs. (8a), (8b) and (8c), k_1, k_2 and k_3 are forward kinetic constant coefficients of the reactions in Eqs. (8a), (8b), and (8c), respectively, *DEN* is a dimensionless parameter and $p_{tube}^{H_2}$, $p_{tube}^{CH_4}$, $p_{tube}^{H_2O}$, p_{tube}^{CO} and $p_{tube}^{CO_2}$ are the partial pressures of H_2, CH_4, H_2O, CO and CO_2 in the tube-side mixture, respectively. This kinetic model is widely accepted (Kuroki et al., 2009) and is frequently used in CFD modeling and first-principles modeling of the SMR process because it accounts for the amount of the available catalyst. The kinetic model can also be modified to account for the external and internal diffusion resistances of the catalyst network by multiplying the kinetic formulas with a universal effectiveness factor of 0.1 (Wesenberg and Svendsen, 2007). However, unlike the global kinetic models of the methane and hydrogen combustion phenomena, because the empirical kinetic formulas shown in Eq. (8) are not in the Arrhenius form, they cannot be directly integrated into the reformer CFD model. Nevertheless, ANSYS Fluent allows these non-Arrhenius form kinetic formulas to be integrated into the CFD model by means of user-defined functions, i.e., *DEFINE_VR_RATE* and *DEFINE_NET_REACTION_RATE*, to simulate the formation and consumption rates of the tube-side components. In Xu and Froment (1989), the complete list of the possible chemical reactions in the SMR process is provided, which does not contain any gas phase reaction. Additionally, the components of the tube-side mixture (i.e., methane, superheated steam, carbon oxides and hydrogen) of the SMR process are naturally stable and will not undergo chemical reaction in the absence of the nickel-based catalyst. Therefore, gas phase reactions are not considered in the present work.

Inside the reforming tubes, the catalyst network with a uniform packing pattern disrupts the tube-side flow and enhances the mixing processes of the tube-side mixture, and the Reynolds number at the reforming tube entrances is calculated to be ~70,000 based on the tube-side feed information detailed in Lao et al. (2016). Therefore, the tube-side flow is expected to be turbulent, and it is necessary to utilize a suitable turbulence-chemistry interaction model to simulate the tube-side species reaction rates under the influence of turbulent effects. Two turbulence-chemistry interaction models offered by ANSYS Fluent that may be appropriate for modeling turbulent effects on the tube-side species reaction rates are the FR/ED model and the eddy dissipation concept (EDC) model. On one hand, the FR/ED model is expected to require less computation time, but is known to estimate observed reaction rates that deviate significantly from experimental data for some reactions with multiple dependent elementary reaction rates (ANSYS Inc., 2013). In contrast, the EDC model is expected to be more accurate because it can utilize detailed multi-step reaction kinetic models to determine the formation and consumption rates of the tube-side species in the turbulent reacting flow, but is computationally expensive. Additionally, the EDC model with default parameters is a robust turbulence-chemistry interaction model, and can be directly applied for a wide variety of reaction-limited and diffusion-limited systems (Magnussen, 2005). The description of the EDC model can be found in ANSYS Inc. (2013). Although the observed reaction rates of the tube-side species calculated from the EDC model are expected to have higher accuracy than those calculated from the FR/ED model of Eq. (3), it is preferable for industrial applications to avoid integrating the EDC model in the reformer CFD model when that does not significantly impact the solution accuracy due to the corresponding increase in the required computational cost. In Section 6, the numerical error associated with the FR/ED model in the solution of the reformer CFD model is evaluated to determine that the FR/ED model is an appropriate chemistry-turbulence interaction model for the tube-side flow.

5.2. Porous zone design

In the reforming tubes, the nickel-based catalyst pellets are used as the packing material, and hence, it is essential to the development of the reformer CFD model that the effects of the catalyst network on the SMR process are well understood. Specifically, the catalyst network facilitates the formation of hydrogen from the naturally stable and slowly-reacting tube-side reactants, i.e., steam and methane, and it also enhances the rate of convective energy transfer from the reforming tube walls to the tube-side mixture by increasing the contact area. Additionally, the catalyst network interferes with the tube-side flow, increases the residence time of the tube-side species and reduces the free volume. Furthermore, a pressure difference between the tube-side mixture at the reforming tube inlet and outlet cannot be neglected due to the presence of the catalyst network inside the reforming tubes. Therefore, the effects of the catalyst on the momentum and energy transport equations of the tube-side must be accounted for. In the present work, the reforming tubes are modeled by the pseudo-homogeneous reactor model in which the solid phase (i.e., the catalyst network) is modeled by the continuum approach, and the effects of the catalyst network on the tube-side flow are modeled by the ANSYS Fluent porous zone function. The porous zone function modifies the standard governing equations of the pseudo-homogeneous reactor model to account for the presence and effects of the catalyst network on the tube-side flow (which will be discussed in Section 7.2). Although the modeling strategy does not require the catalyst pellets and the random packing pattern of the catalyst network to be modeled, the simulation data generated by the reforming tube CFD model is expected to capture the gradients of the tube-side composition and state variables at the macroscopic scale typically larger than the equivalent

dimension of the catalyst pellet (Mokheimer et al., 2015). The modeling strategy has been shown to be valid for packed-bed reactors in which the effective characteristic dimension of the catalyst pellets is less than 5 mm (Seo et al., 2006). We have found that a reforming tube CFD model created from this modeling approach can simulate the macroscopic effects of the catalyst network on the tube-side mixture (e.g., the pressure drop across the catalyst network and the increase of the tube-side residence time generated by the reforming tube CFD model are consistent with the typical plant data) (Lao et al., 2016). In the reformer CFD model, the modeling parameters of the porous zone function are estimated from the semi-empirical Ergun equation (Ergun and Orning, 1949):

$$\frac{\Delta P_{tube}}{L_{tube}} = \frac{150\mu_{tube}}{D_p^2}\frac{(1-\gamma)^2}{\gamma^3}v_{\infty,tube} + \frac{1.75\rho_{tube}}{D_p}\frac{(1-\gamma)}{\gamma^3}v_{\infty,tube}^2 \tag{9}$$

where ΔP_{tube} (kPa) is the pressure difference of the tube-side mixture across the catalyst network, $v_{\infty,tube}$ (m s^{-1}), ρ_{tube} (kg m^{-3}) and μ_{tube} (kg m^{-1} s^{-1}) are the average superficial velocity, density and viscosity of the tube-side mixture at the reforming tube inlet and outlet, respectively, L_{tube} of 12.5 m is the reforming tube length, $\gamma = 0.609$ is the porosity of the catalyst network and D_p (m) is an effective diameter of the catalyst pellets. Based on the pressure drop of the tube-side mixture across the catalyst network from typical plant data, reforming tube geometry and available physical properties of the catalyst network reported in Lao et al. (2016), the Ergun equation is employed to estimate the effective diameter of the catalyst pellets. Then, the modeling parameters of the porous zone function required by the reformer CFD model are calculated as follows,

$$\alpha = \frac{D_p^2}{150}\frac{\gamma^3}{(1-\gamma)^2} \tag{10a}$$

$$\beta = \frac{3.5}{D_p}\frac{(1-\gamma)}{\gamma^3} \tag{10b}$$

where $\alpha^{-1} \sim 8,782,800$ m^{-2} is the viscous resistance coefficient of the catalyst network and $\beta \sim 1,782$ m^{-1} is the inertial resistance coefficient of the catalyst network. It is noteworthy that because the semi-empirical Ergun equation is suitable for a wide range of Reynolds numbers and various packing patterns (ANSYS Inc., 2013), it is not necessary to model the detailed packing of the catalyst network within the reformer. In this CFD model, the catalyst network inside each reforming tube is assumed to have a uniform packing structure and to be functioning properly (i.e., no deactivation or sintering occurs). Hence, the coefficients of viscous resistance and inertial resistance of the catalyst network can be assumed to be constant and uniform along the axial and radial directions.

6. Equation of state and turbulence-chemistry interaction model

In this section, we present the procedure by which the thermodynamic and turbulence-chemistry interaction models are selected for the reformer CFD model. The modeling considerations that motivate the analysis of multiple equations of state and turbulence-chemistry interaction models are discussed. Finally, a strategy to obtain the necessary numerical evidence, which is subsequently analyzed to determine the solutions for the modeling challenges, is proposed.

The first modeling consideration is the choice of an equation of state for describing the thermodynamics of the furnace-side and tube-side flows in the reformer. In the combustion chamber of the reformer, the maximum temperature of the furnace-side mixture is approximately 2050 K due to the thermal energy released by the rapid oxidation of the furnace-side feed, and the operating pressure is designed to be nearly at atmospheric pressure at ~132 kPa. Therefore, the furnace-side mixture can be assumed to possess incompressible ideal gas characteristics. On the contrary, the thermodynamic behavior of the tube-side mixture is speculated to deviate significantly from that governed by the incompressible ideal gas law due to the high operating pressure inside the reforming tubes (i.e., ~3000 kPa), which is ~25–28 times higher than that of the combustion chamber (Latham, 2008). Specifically, the tube-side density at high operating pressure of the reforming tubes is expected to be significantly different from the estimated density by the incompressible ideal gas law using the reference state of 298 K. It is critical to the development of the reformer CFD model that the adopted equation of state accurately predicts the thermodynamics of turbulent reacting flows inside both the combustion chamber and reforming tubes because the SMR process is expected to reach equilibrium at the reforming tube outlets. In an effort to choose an appropriate equation of state, two potential thermodynamic models, i.e., the compressible ideal gas and the real gas Soave-Redlich-Kwong (SRK) equations of state, are selected. It is important to note that the real gas SRK model predicts more accurate fluid properties than the compressible ideal gas model and is frequently employed for determining fluid thermodynamic properties for industrial applications. Nevertheless, the required computational cost of the real gas SRK model is higher than that of the compressible ideal gas model; the former thermodynamic model should be integrated into the reformer CFD model only when the latter model is proven to be inadequate for obtaining accurate results.

The second modeling consideration is the selection of an appropriate turbulence-chemistry interaction model. As discussed in Sections 4.1 and 5.1, the FR/ED and EDC models are two viable models for these phenomena, but the FR/ED model may produce inaccurate results, though it is expected to have a lower computational time than the EDC model.

To evaluate whether the less computationally intensive modeling strategies (compressible ideal gas and FR/ED models) can be expected to produce sufficiently accurate results, we could develop one reformer CFD model that uses the more computationally intensive modeling strategies (i.e., the SRK and EDC models) and one that uses the less computationally intensive modeling strategies. The results could then be compared to analyze the impact on the CFD numerical results of utilizing the more rigorous SRK and EDC models compared to utilizing the less accurate (but more suitable in terms of computational cost, computing time, and memory capacity for industrial applications) compressible ideal gas and FR/ED models. Nevertheless, the available computational power (i.e., 80 cores on UCLA's Hoffman2 Cluster) and memory capacity (i.e., 20.0 GB on UCLA's Hoffman2 Cluster) are not expected to be sufficient to simulate the reformer CFD model with the more computationally intensive modeling strategies in a timely manner because the reformer mesh is composed of 29,099,252 hexahedral grids, 88,798,168 quadrilateral faces and 30,584,930 nodes. Consequently, it is not practical to employ the reformer CFD model that uses the more computationally intensive modeling strategies as a means to obtain the necessary numerical evidence, which would subsequently be used as a basis for selection of the appropriate models. As an alternative for assessing the expected order of magnitude of differences in the CFD numerical results when employing the more computationally intensive versus less computationally intensive modeling strategies, we would like to use a part of the reformer domain (e.g., a single reforming tube) to analyze both types of thermodynamic and chemistry-turbulence interaction models. However, the transport phenomena of the reforming tubes of the reformer CFD model are coupled and thus a single reforming tube from the reformer model could not be simulated individually. Therefore, a CFD model

of a single industrial-scale reforming tube developed from our previous work (Lao et al., 2016) using modeling strategies similar to those employed for modeling the reforming tubes of the reformer CFD model is readily available and will be used in the remainder of this section for assessing whether the more or less computationally intensive modeling strategies will be chosen for the reformer CFD model.

Before utilizing the industrial-scale reforming tube from Lao et al. (2016) to assess the appropriateness of the more and less computationally intensive thermodynamic and turbulence-chemistry interaction models for the reformer CFD model, the differences between the industrial-scale reforming tube mesh and modeling strategies and those of the reformer CFD model are discussed to demonstrate the large reduction in the computation time offered by the industrial-scale reforming tube CFD model. Three key differences between the reformer mesh and industrial-scale reforming tube mesh are the shape of the subdomains, the number of the subdomains and the mesh quality. Specifically, the industrial-scale reforming tube mesh developed in Lao et al. (2016) is the 2-D axisymmetric quadrilateral structured mesh, and the reformer CFD mesh is the 3-D hexahedral structured mesh. Additionally, the industrial-scale reforming tube mesh consists of ~23 thousand subdomains, and the reformer mesh has ~29 million subdomains, which corresponds to a cell count that is ~1264 times higher than that of the former mesh. Moreover, the mesh quality of the industrial-scale reforming tube mesh reported in Lao et al. (2016) is nearly ideal based on the three suggested criteria (i.e., the orthogonal factor, aspect ratio and ortho skew) and is better than that of the reformer mesh shown in Table 1. Therefore, the industrial-scale reforming tube CFD model serves as an effective tool to quantify the magnitude of the numerical error introduced in the CFD simulation data when the computationally less intensive modeling strategies (i.e., the compressible ideal gas model and the FR/ED model) are implemented, and the industrial-scale reforming tube CFD model is expected to have a faster speed of convergence than that of the reformer CFD model, making the analysis possible in a reasonable time frame.

In this effort, two industrial-scale reforming tube CFD models are developed, one of which utilizes the SRK and EDC models, and the other of which uses the compressible ideal gas and FR/ED models (for brevity, the former and latter CFD models will be referred to as the original and simplified tube CFD models, respectively). In this study, all boundary conditions of the tube CFD models (i.e., the outer reforming tube wall temperature and the tube-side feed conditions) are derived from typical plant data (Lao et al., 2016), and the modeling strategies are identical to those of the reformer CFD model. The simulation results generated by the original and simplified tube CFD models are shown in Table 5. The deviations of the simulation results generated by the simplified tube CFD model with respect to the data generated by the original tube CFD model are considered to be insignificant. However, the computational benefits of utilizing the simplified tube CFD model compared to using the original tube CFD model are noticeable. Specifically, the original tube CFD model takes 1100 iterations and 650 s of computing time to reach the converged solution, while the simplified tube CFD model only takes 871 iterations and 320 s. This result shows that the simplified tube CFD model offers a 20% reduction in the number of iterations and a 50% reduction in the computing time required for the simulation to reach the converged solution and yields similar simulation data compared to the original tube CFD model. As a result, the compressible ideal gas and FR/ED models are integrated in the reformer CFD model to describe the thermodynamics and reaction rates of individual species in the turbulent reacting flows of both the tube-side and furnace-side mixtures.

Table 5
Simulation results of the original and simplified tube CFD models in which $\overline{P}_{tube,inlet}$ and $\bar{x}^{i}_{tube,outlet}$ represent the radial-weighted average inlet pressure and outlet mole fraction of species i in the tube-side mixture.

	Original tube CFD model [∗]	Simplified tube CFD model	Difference (%, with respect to ∗)
ΔP_{tube} (kPa)	204.2	210.3	3.00
$\overline{P}_{tube,inlet}$ (kPa)	2958.2	2964.3	0.21
Average heat flux (kW m^{-2})	69.506	68.423	1.56
$\bar{x}^{H_2}_{tube,outlet}$	0.470	0.469	0.33
$\bar{x}^{H_2O}_{tube,outlet}$	0.341	0.341	0.00
$\bar{x}^{CH_4}_{tube,outlet}$	0.043	0.044	3.44
$\bar{x}^{CO}_{tube,outlet}$	0.088	0.087	1.18
$\bar{x}^{CO_2}_{tube,outlet}$	0.058	0.059	1.43

Remark 1. The most prominent difference in the modeling strategies of the industrial-scale reforming tube mesh and of a reforming tube in the reformer CFD model is that the industrial-scale reforming tube assumes a tube wall temperature profile along the reforming tube length whereas the reforming tubes in the reformer exhibit a temperature profile dependent on the furnace-side environment which is simultaneously calculated. Though these differences in the mesh and modeling strategies exist, they are not expected to significantly impact the order of magnitude of numerical differences in the CFD results for the industrial-scale reforming tube using the more and less computationally intensive modeling strategies compared to the order of magnitude of the differences that would be observed using a reforming tube from the reformer model. Furthermore, the order of magnitude of the results utilizing a single reforming tube would be expected to be indicative of the order of magnitude of differences that would be expected on the furnace-side as well, particularly since the equation of state is not expected to pose an issue on the furnace side due to the relatively low pressures in that domain.

7. Governing equations of industrial-scale SMR unit

The reformer mathematical model consists of two sets of highly non-linear coupled partial integro-differential equations with seven independent variables as discussed in Section 1. Specifically, one of the two equation sets represents the combustion chamber model, and the other is the reforming tube model. In this section, we present the equations of continuity and of momentum, energy, and species material conservation that employ parameters or variables calculated from the modeling strategies discussed in the prior sections to characterize the mass, flow, heat and species transport within the reformer. The physical properties of individual species in these equations in the tube-side and furnace-side mixtures are imported from the ANSYS Fluent database materials. Subsequently, the physical properties of the tube-side and furnace-side mixtures are computed based on those of the corresponding constituents, ideal gas mixing law (in the case of the thermal conductivities and viscosities) and kinetic theory (in the case of the diffusion coefficients). Inside the combustion chamber and reforming tubes, the flow profiles are speculated to be turbulent as discussed in Sections 4.1 and 5.1, and thus, the state variables (e.g., temperature, pressure, internal energy, enthalpy, and entropy) and fluid properties (i.e., velocity, density and species concentration) fluctuate about their corresponding time-averaged values. In the present work, the standard $k-\epsilon$ turbulence model developed from the Reynolds-averaged Navier–Stokes (RANS) equations and the Boussinesq hypothesis is integrated in the reformer CFD

model to characterize the furnace-side and tube-side turbulent reacting flows, which allows the reformer CFD model to simulate the effects of turbulence on the transport and chemical reaction phenomena (Jones and Launder, 1972; Launder and Sharma, 1974; ANSYS Inc., 2013). The standard $k-\epsilon$ model is selected because it is a robust turbulence model, it requires lower computational resources compared to the realizable $k-\epsilon$ model (i.e., relatively longer computing time), RNG $k-\epsilon$ model (i.e., 15% more computing time) and Reynolds stress model (i.e., 50–60% more computing time), and it is expected to yield reasonably accurate predictions for a wide range of turbulent flows (ANSYS Inc., 2013). Additionally, the standard $k-\epsilon$ model is expected to be suitable when there are not extreme pressure gradients within the fluid (ANSYS Inc., 2013), which we do not expect to observe on either the tube side or furnace side of the reformer because the ratios between the pressure drop and the inlet pressure of the tube-side feed and furnace-side feed are ~5% and ~0%, respectively, based on the typical plant data (Latham, 2008). In the present work, the enhanced wall treatment option of the standard $k-\epsilon$ model is used to improve the model accuracy at the regions near the walls. Therefore, though the ideal dimensionless distance from the wall to the first interior node (denoted by y+) everywhere in the reformer mesh is recommended by ANSYS Fluent to be ~1, the use of the standard $k-\epsilon$ model with enhanced wall treatment allows the accuracy of the CFD data to be less sensitive to the y+ value, which allows for the y+ value of the reformer mesh to be greater than 1 and allows the cell count in the reformer mesh to be reduced compared to the case that the y+ value is ~1. In the present work, the initial guess of the grid size is obtained from NASA's viscous grid spacing calculator based on the Reynolds number of the furnace-side mixture at the inner-lane burner inlet (Re = 240,000), the diameter of the inner-lane burner inlet and the desired value of y+, which varies between 30 and 60. The grid size is further adjusted by a trial-and-error approach during the trial simulations of the reformer CFD model to ensure that the convergence criteria defined in Section 8 can be reached. From the simulation results, the average y+ values at the outer reforming tube wall and the interior wall of the combustion chamber obtained from the CFD simulation data were 20.8 and 58.9, respectively. The reformer mathematical model accounts for transport phenomena frequently observed in high-operating-temperature applications in addition to the essential reformer-related considerations discussed in Sections 4.1, 4.2, 5.1 and 5.2. In the remainder of this section, the combustion chamber model and the reforming tube model are presented.

7.1. Furnace chamber

The combustion chamber model developed in this work can simulate the mixing-controlled characteristics of non-premixed combustion phenomena, radiative heat transfer between the furnace-side mixture, outer reforming tube walls and combustion chamber refractory inner walls, in addition to other heat transfer mechanisms observed in reformers (e.g., convective and conductive heat transfer). Based on the above considerations and those discussed in Sections 4 and 6, the combustion chamber model including the continuity equation (Eq. (11a)), the momentum (Eq. (11b)), energy (Eq. (11c)) and species (Eq. (11d)) conservation equations, and the turbulence model (Eqs. (11e) and (11f)) required for characterizing the heat and fluid-flow fields as well as composition inside the combustion chamber are formulated as follows:

Continuity equation:

$$\frac{\partial}{\partial t}(\rho_{comb}) + \nabla\cdot(\rho_{comb}\vec{v}_{comb}) = 0 \tag{11a}$$

Momentum conservation equation:

$$\frac{\partial}{\partial t}(\rho_{comb}\vec{v}_{comb}) + \nabla\cdot(\rho_{comb}\vec{v}_{comb}\vec{v}_{comb}) = -\nabla P_{comb} + \nabla\cdot\bar{\bar{\tau}}_{comb} + \rho_{comb}\vec{g} \tag{11b}$$

Energy conservation equation:

$$\frac{\partial}{\partial t}(\rho_{comb}E_{comb}) + \nabla\cdot(\vec{v}_{comb}(\rho_{comb}E_{comb}+P_{comb})) = \nabla\cdot\left[k^{eff}_{comb}\nabla T_{comb} - \left(\sum_i h^i_{comb}\vec{J}^i_{comb}\right) + \left(\bar{\bar{\tau}}_{comb}\cdot\vec{v}_{comb}\right)\right] + S^{h,rxn}_{comb} + \nabla\cdot\vec{q}_{rad} \tag{11c}$$

Species material conservation equation:

$$\frac{\partial}{\partial t}(\rho_{comb}Y^i_{comb}) + \nabla\cdot(\rho_{comb}\vec{v}_{comb}Y^i_{comb}) = -\nabla\cdot(\vec{J}^i_{comb}) + R^i_{comb} \tag{11d}$$

Transport equations of the standard $k-\epsilon$ turbulence model:

$$\frac{\partial}{\partial t}(\rho_{comb}k_{comb}) + \nabla\cdot(\rho_{comb}k_{comb}\vec{v}_{comb}) = \nabla\cdot\left[\left(\mu_{comb}+\frac{\mu^t_{comb}}{\sigma_k}\right)\nabla k_{comb}\right] + G^k_{comb} + G^b_{comb} - \rho_{comb}\epsilon_{comb} \tag{11e}$$

$$\frac{\partial}{\partial t}(\rho_{comb}\epsilon_{comb}) + \nabla\cdot(\rho_{comb}\epsilon_{comb}\vec{v}_{comb}) = \nabla\cdot\left[\left(\mu_{comb}+\frac{\mu^t_{comb}}{\sigma_\epsilon}\right)\nabla\epsilon_{comb}\right] + C_{1\epsilon}\frac{\epsilon_{comb}}{k_{comb}}G^k_{comb} - C_{2\epsilon}\rho_{comb}\frac{\epsilon^2_{comb}}{k_{comb}} \tag{11f}$$

$$\vec{J}^i_{comb} = \left(\rho_{comb}D^{m,i}_{comb} + \frac{\mu^t_{comb}}{Sc^t_{comb}}\right)\nabla Y^i_{comb} \tag{12a}$$

$$\bar{\bar{\tau}}_{comb} = \mu_{comb}\left[(\nabla\vec{v}_{comb} + \nabla\vec{v}^T_{comb}) - \frac{2}{3}\nabla\cdot\vec{v}_{comb}I\right] \tag{12b}$$

$$E_{comb} = h_{comb} + \frac{v^2_{comb}}{2} - \frac{P_{comb}}{\rho_{comb}} \tag{12c}$$

$$h_{comb} = \sum_j Y^j_{comb}h^j_{comb} \tag{12d}$$

$$h^j_{comb}(T_{comb}) = \int_{T_{ref}}^{T_{comb}} C^j_{p,comb}dT \text{ with } T_{ref} = 298.15\text{ K} \tag{12e}$$

$$S^{h,rxn}_{comb} = -\sum_j \frac{h^f_j}{M_j}R^j_{comb} \tag{12f}$$

$$R^j_{comb} = \sum_k^3 \nu^{k,j}_{comb}R^{k,j}_{comb} \tag{12g}$$

$$k^{eff}_{comb} = k^l_{comb} + k^t_{comb} \tag{12h}$$

$$k^t_{comb} = \frac{C_{p,comb}\mu^t_{comb}}{Pr_t} \tag{12i}$$

$$\mu^t_{comb} = \rho_{comb}C_\mu\frac{k^2_{comb}}{\epsilon_{comb}} \tag{12j}$$

$$G^k_{comb} = -\rho_{comb}\overline{v'_{comb,i}v'_{comb,j}}\frac{\partial v_{comb,j}}{\partial x_i} \tag{12k}$$

$$G^b_{comb} = \beta' g_i\frac{\mu^t_{comb}}{Pr_t}\frac{\partial T_{comb}}{\partial x_i} \tag{12l}$$

where $\vec{v}_{comb}$ (m s^{-1}), μ_{comb} (kg m^{-1} s^{-1}), μ^t_{comb} (kg m^{-1} s^{-1}), k^{eff}_{comb} (W m^{-1} K^{-1}), k^l_{comb} (W m^{-1} K^{-1}), k^t_{comb} (W m^{-1} K^{-1}), $C_{p,comb}$

($J\,kg^{-1}\,K^{-1}$), T_{comb} (K) and P_{comb} (kPa) are the furnace-side mixture mass-averaged velocity, laminar mixture viscosity, turbulent mixture viscosity (calculated as shown in Eq. (12j)), effective thermal conductivity (estimated as shown in Eq. (12h)), laminar thermal conductivity, turbulent thermal conductivity (estimated as shown in Eq. (12i)), specific heat capacity, temperature and pressure of the furnace-side mixture in the combustion chamber, respectively, $\vec{g}$ is the universal gravitational acceleration, $\overline{\overline{\tau}}_{comb}$ is the stress tensor (estimated as shown in Eq. (12b)), and I is the unit tensor. The combustion chamber model accounts for all reformer-relevant modes of momentum, energy and material transport phenomena under the influence of chemical phenomena and turbulence to characterize the dynamics of the chamber. Specifically, the turbulent mass diffusion flux of species i, $\vec{J}^{i}_{comb}$, driven by concentration gradients, is shown in Eq. (12a), where Y^{i}_{comb} and $D^{m,i}_{comb}$ are the furnace-side mass fraction and laminar mass diffusion coefficient of species i, respectively. It is necessary to note that the ratio $\frac{\mu^{t}_{comb}}{Sc^{t}_{comb}}$, in which Sc^{t}_{comb} and μ^{t}_{comb} are the turbulent Schmidt number and turbulent viscosity of the furnace-side mixture, is used to account for the effect of turbulence on the mass diffusion flux of species i, and therefore, it can be written as$\rho_{comb}D^{m,t}_{comb}$ where $D^{m,t}_{comb}$ is the turbulent mass diffusion coefficient. Additionally, the specific internal energy (E_{comb}) of the furnace-side mixture which can be computedas the sum of the furnace-side specific sensible enthalpy (h_{comb}) which depends on the furnace-side specific sensible enthalpy of species j at temperature T_{comb} ($h^{j}_{comb}(T_{comb})$), specific kinetic energy ($v^{2}_{comb}/2$) and external work per unit weight of the furnace-side mixture ($-P_{comb}/\rho_{comb}$), is shown in Eqs. (12c), (12d) and (12e). It is important to note that the value of $T_{ref} = 298.15$ K in Eq. (12e) is chosen automatically by ANSYS Fluent's parallel/pressure based solver, and $C^{j}_{p,comb}$ is the heat capacity of species j in the combustion chamber. In addition, from Eq. (11c), $\nabla\cdot(k^{eff}_{comb}\nabla T_{comb})$, $-\nabla\cdot\left(\sum_i h^{i}_{comb}\vec{J}^{i}_{comb}\right)$, $\nabla\cdot(\overline{\overline{\tau}}_{comb}\cdot\vec{v}_{comb})$ and $\nabla\cdot\vec{q}_{rad}$ represent four distinct mechanisms, i.e., conduction, species diffusion, viscous dissipation and radiation, respectively, through which energy is transferred. Furthermore, the overall rate at which thermal energy is released from combustion processes inside the combustion chamber, $S^{h,rxn}_{comb}$, is computed as shown in Eq. (12f) in which R^{j}_{comb} and h^{f}_{j} represent the overall volumetric consumption/formation rate and enthalpy of formation of species j, and $v^{k,j}_{comb}$ and $R^{k,j}_{comb}$ are the stoichiometric coefficient and volumetric consumption/formation rate of species j in reaction k. It is noteworthy that $R^{k,j}_{comb}$ is determined by the FR/ED turbulence-chemistry interaction model (Section 4.1). Transport equations of the standard $k-\epsilon$ turbulence model are presented in Eqs. (11e) and (11f), in which k_{comb} and ϵ_{comb} are the turbulence kinetic energy and turbulence dissipation rate of the furnace-side mixture, β' is the coefficient of thermal expansion of the furnace-side mixture, $\sigma_k = 1.3$ and $\sigma_\epsilon = 1.0$ are the default values of the turbulent Prandtl numbers for k_{comb} and ϵ_{comb}, $C_{1\epsilon} = 1.44$, $C_{2\epsilon} = 1.92$, $C_\mu = 0.09$ and $Pr_t = 0.85$ are default constants of the standard $k-\epsilon$ turbulence model, respectively, and G^{k}_{comb} and G^{b}_{comb} represent the generation of turbulence kinetic energy in the furnace-side mixture due to the mean velocity gradients (Eq. (12k)) and buoyancy effect (Eq. (12l)). The standard $k-\epsilon$ turbulence model can capture the characteristic parameters of turbulent reacting flow profiles. Specifically, in Eq. (12k), the term $-\rho_{comb}\overline{v'_{comb,i}v'_{comb,j}}$ is the Reynolds stress representing the effect of turbulence on the velocity profile of the furnace-side mixture that arises from the RANS equations, and $\overline{v'_{comb,i}}$ is the time-averaged fluctuating component of $\vec{v}_{comb}$ in the x_i direction. It is worth noting that all default constants of the standard $k-\epsilon$ turbulence model are determined empirically by experiments for fundamental turbulent flows, and have been shown to be suitable for a wide range of wall-bounded and free shear flow applications (ANSYS Inc., 2013). Table 8, which includes the paper notation, summarizes the notation described above.

7.2. Reforming tube

In the present work, the effects of the catalyst network on the tube-side transport phenomena are accounted for by the ANSYS Fluent porous zone function, which includes the additional momentum sink term in the momentum conservation equation of the reforming tube model to simulate the interference effect of the catalyst network, which decreases the superficial velocity and increases the residence time of the tube-side species. In addition, the energy conservation equation of the reforming tube model is affected by the porous zone function to include an additional transient term to account for the thermal inertia of the catalyst network and to use the effective thermal conductivity to account for the presence of the catalyst network. Moreover, the tube-side species material balances of the reforming tube model use the overall effectiveness factor (η) to account for the internal and external mass transfer resistances of the catalyst network and the catalyst packing factor ($(1-\gamma)\rho_{cat}$) to convert the surface reaction rates from Eq. (8) to volumetric reaction rates (i.e., $kg\,m^{-3}\,h^{-1}$) that are employed within the FR/ED turbulence-chemistry interaction model for use within the species material balances. These approximations of the effects of the catalyst network on the transport equations and species balances were also utilized in the development of the industrial-scale reforming tube CFD model for which the simulation results have been shown to be in good agreement with typical plant data (Lao et al., 2016), and thus these approximations are expected to be sufficient for the reforming tubes of the reformer CFD model. The reforming tube walls are modeled by the ANSYS Fluent thin wall model in which the thermal resistance of the reforming tube wall and the temperature profile across the reforming tube wall thickness can be estimated without meshing the reforming tube wall explicitly. In the simulation of the reforming tube CFD model, the ANSYS Fluent thin wall model creates an artificial wall thickness for the reforming tubes, and the ANSYS Fluent solver utilizes the 1-D steady heat conduction equation to determine the reforming tube wall thermal resistance based on the specified artificial wall thickness and material of the reforming tubes. This modeling strategy is utilized because the wall thickness is negligible compared to other dimensions of the system (the ratio of the reforming tube exposed length and wall thickness is ~1250:1, and the ratio of the reforming tube diameter and wall thickness is ~13:1). This modeling strategy for the tube wall affects the boundary conditions of the reforming tube walls when solving the heat transfer equations. Radiation is neglected in the energy balance equation for the tube side (Seo et al., 2006; Kuroki et al., 2009; Mokheimer et al., 2015) because the nickel-based catalyst network expands the contact area between the tube-side mixture and the inner reforming tube wall, with the result that convective heat transfer is expected to be the dominant mode. Based on the above considerations and those discussed in Sections 5 and 6, the governing equations including the continuity equation and the momentum, energy and tube-side species balances, and the turbulence model required to simulate the SMR process inside the reforming tubes, are constructed in a similar manner to that of the combustion chamber, which has been described in Section 7.1. Additionally, the governing equations of the tube-side mixture have also been explicitly presented in our recent publication (Lao et al., 2016), and therefore, they are not repeated here for brevity.

8. Process simulation

Intuitively, the CFD solution of the reformer CFD model would be obtained by simulating the reformer CFD model until convergence criteria are satisfied. However, the reformer CFD model has been found to be very sensitive to the initial guess (e.g., the simulation of the reformer CFD model with the initial guess automatically generated by the ANSYS Fluent standard initialization function based on the boundary conditions of the CFD model is often unstable and is likely to quickly diverge). Although ANSYS Fluent allows a conservative mode of the ANSYS Fluent solver to be selected to prevent the reformer CFD simulation from diverging, this strategy often results in a substantial increase in the required computing time to calculate the converged solution of the reformer CFD model, and therefore, forfeits the potential of the reformer CFD model for industrial interests. In this work, a step-by-step converging strategy that allows the implementation of an aggressive mode of the ANSYS Fluent solver to compute the reformer CFD steady-state solution is proposed as shown in Fig. 5. Specifically, the step-by-step converging strategy is an optimized procedure that is designed to resolve the instability issue of the reformer CFD simulation, to accelerate the rate of convergence and to minimize the required computing time to obtain the converged solution of the reformer CFD model. Initially, an isothermal, non-reacting (INR) reformer CFD model is created by deactivating the combustion phenomena, radiative heat transfer and SMR kinetic models in addition to excluding the energy conservation equations from the furnace-side and tube-side models. Then, the simulation of the INR reformer CFD model is initialized with the initial guess generated by the ANSYS Fluent standard initialization function based on the tube-side and furnace-side feeds, and is solved by the aggressive mode of the ANSYS Fluent solver. In this work, the reformer CFD simulation is said to reach the converged solution when the global normalized residuals of all transport variables computed over all subdomains of the reformer between two consecutive iterations are less than 10^{-4}, the mass flow rate integrated over all boundaries of the reformer CFD model is approximately zero, the total heat transfer rate integrated over all boundaries of the reformer CFD model is less than 1% of the reformer total fired duty and the absolute residuals of the furnace-side temperature at five different locations inside the combustion chamber are less than 1 K. Next, the converged solution of the INR reformer CFD model is utilized as an initial guess for the succeeding non-reacting (NR) CFD model because even though the composition and temperature fields in the INR reformer CFD model are different from those in the NR reformer CFD model, their velocity and turbulence fields are expected to be similar (ANSYS Inc., 2013; Vuthaluru and Vuthaluru, 2006). Analogously, the converged reformer CFD solution in each preceding step is utilized as an initial guess for the reformer CFD model in the subsequent step until the converged solution of the complete reformer CFD model is obtained.

The solution of the reformer CFD model is obtained after ~72 h of computing time by the ANSYS Fluent parallel solver with a computational power of 80 cores on UCLA's Hoffman2 Cluster. During the initialization procedure of the reformer CFD model, the ANSYS Fluent solver arbitrarily selects one of the available 80 cores as a host process and designates the remaining 79 cores as compute-node processes. It is noteworthy that the host process is only responsible for interpreting the user's commands given in the graphical user interface (GUI), then redistributing them to all compute-node processes by a message-passing library, e.g., the Message Passing Interface (MPI). Thus, the reformer mesh is partitioned into 79 parts corresponding to the number of available compute-node processes, and each partition consisting of

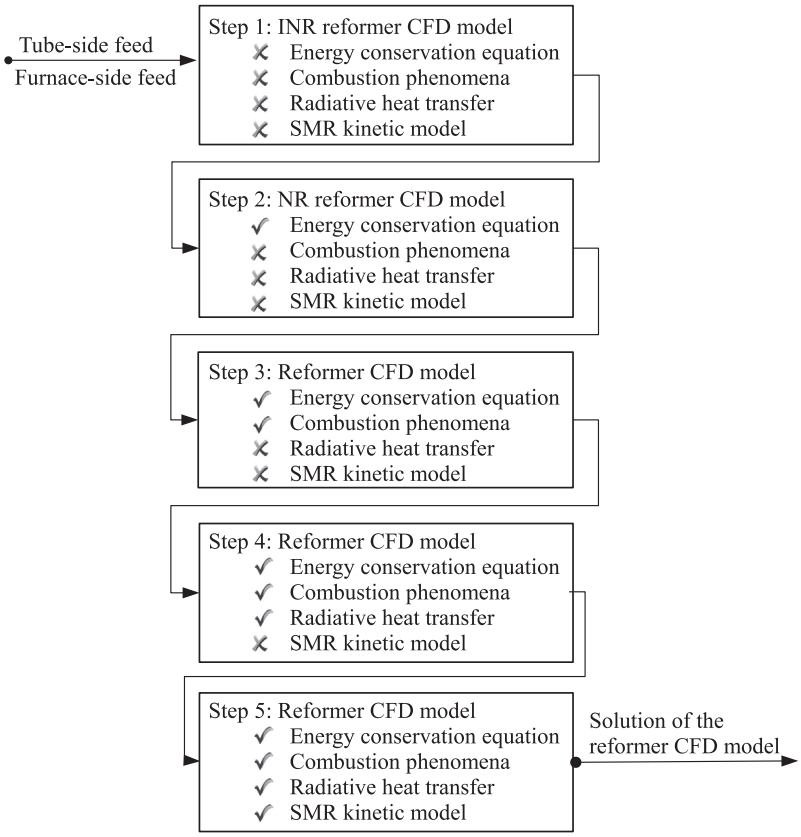

Fig. 5. Step-by-step converging strategy designed to resolve the initial instability issue of the reformer CFD simulation, accelerate the rate of convergence and minimize the required computing time to obtain the converged solution of the reformer CFD model in which the models with ✓ are activated, and those with ✗ are disabled.

~368,345 grids is assigned to a different compute-node process. Then, the compute-node processes consider each grid within the corresponding partitions as an open system in which the reformer mathematical model is discretized by the finite differences method and numerically solved until the convergence criteria are satisfied. The corresponding solutions of the grids are recombined to generate the simulation results of the reformer CFD model.

9. Simulation results

In this section, the steady-state simulation results of the reformer CFD model with the furnace-side and tube-side operating conditions and properties as shown in Tables 2–6 are presented.

Two cross-sectional planes (i.e., the frontal and lateral planes) of the combustion chamber as shown in Fig. 6 are designated along which the properties of the furnace-side mixture are presented. Specifically, the furnace-side temperature contour maps (lateral and frontal planes) are shown in Fig. 7. The contour maps of the thermal energy released by the oxidation of the furnace-side feed are shown in Fig. 8. In addition, the furnace-side velocity magnitude vector plots are shown in Fig. 9, and the furnace-side species contour maps are shown in Figs. 10–13.

The properties of the interior of a reforming tube are displayed for a cross-sectional plane along the axial direction of a reforming tube. Because the dimension of the heated reforming tube length is ~85 times longer than that of the reforming tube diameter, the radial dimension of the reforming tube cross section is scaled up by 20 times for display purposes. The tube-side pressure contour map is shown in Fig. 14. The radially uniform pressure profile inside the reforming tubes is the result of the uniformly packed catalyst network assumption, and the definition of the porous zone with uniform coefficients of viscous resistance and inertial resistance of the catalyst network along the axial and radial directions as presented in Section 5.2.

Lastly, the average composition profiles of the tube-side mixture are shown in Fig. 15, and the average temperature profiles of the outer and inner reforming tube walls and the furnace-side and tube-side mixtures are shown in Fig. 16. Fig. 16 suggests that the maximum temperature of the outer reforming tube wall of ~1180 K is below the maximum allowable operating temperature of ~1300 K (Rostrup-Nielsen and Rostrup-Nielsen, 2002); if the outer reforming tube wall were to exceed the maximum temperature for a sufficient length of time, the reforming tube would rupture more quickly than if it were kept below this maximum temperature.

10. Discussion

In computational fluid dynamics study, a converged solution is not necessarily a physically correct solution, and therefore, the simulation results produced by the reformer CFD model are inspected by the well-established knowledge of the phenomena typically observed in reformers and validated by the typical plant data (Latham, 2008; Latham et al., 2011, Rostrup-Nielsen, 1984; Dybkjaer, 1995; Froment and Bischoff, 1990; Pantoleontos et al., 2012) in the remainder of this section.

We begin by checking that the modeling strategies employed produced the effects expected. For instance, the furnace-side feed composition in Table 2 indicates that it is lean-fuel (i.e., the ratio of air to fuel of the furnace-side feed is higher than the stoichiometric ratio). Therefore, it is expected that the fuel will be fully oxidized and that oxygen will remain in the flue gas. Figs. 10, 11 and 12 demonstrate that the composition of the furnace-side reducing agents in the CFD solution are effectively zero everywhere except in the reaction zones, and Fig. 13 shows that oxygen is not completely consumed, as expected. Additionally, the characteristics of non-premixed combustion phenomena that are expected in the furnace-side as discussed in Section 4.1 can be observed in the converged reformer CFD solution. In particular, Figs. 10–12 reveal that the furnace-side compositions in the vicinities of the inner-lane and outer-lane burners are almost identical to those in the furnace-side feed, and Fig. 8 shows that the oxidation rate of the furnace-side feed in these regions is close to zero. These results suggest that the reformer CFD model correctly simulates the initial mixing of the fuel and air streams of the furnace-side feed, in which the observed oxidation rate of the furnace-side species is expected to be relatively slow. Moreover, the characteristics of

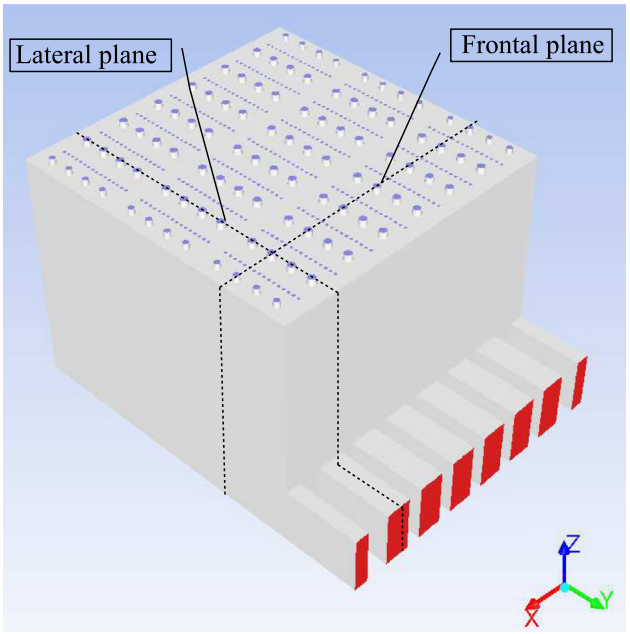

Fig. 6. The frontal and lateral cross-sectional plane of the combustion chamber.

Table 6
Validation of reformer CFD model.

	Industrial-scale reforming tube CFD model	Reformer CFD model	Reforming Gibbs reactor model	Typical plant data (Latham, 2008)
ΔP_{tube} (kPa)	194.29	106.22	N/A	146.9
$\bar{P}_{tube,outlet}$ (kPa)	2955.2	3044.0	N/A	2879.8
Average heat flux (kW m^{-2})	70.659	69.523	N/A	67.125
$\bar{x}^{H_2}_{tube,outlet}$	0.4734	0.4687	0.4686	0.4713
$\bar{x}^{H_2O}_{tube,outlet}$	0.3380	0.3419	0.3411	0.3377
$\bar{x}^{CH_4}_{tube,outlet}$	0.0389	0.0430	0.0433	0.0453
$\bar{x}^{CO}_{tube,outlet}$	0.0905	0.0883	0.0872	0.0889
$\bar{x}^{CO_2}_{tube,outlet}$	0.0574	0.0576	0.0589	0.0559

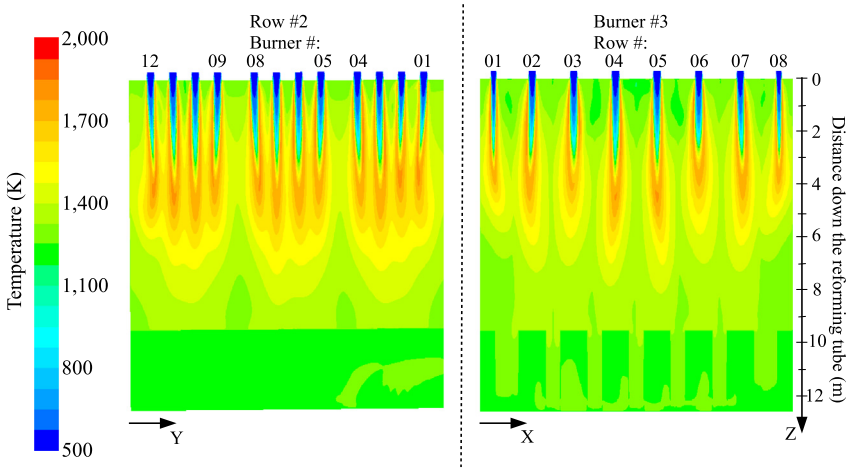

Fig. 7. Lateral (left) and frontal (right) furnace-side temperature contour maps predicted by the reformer CFD simulation in which the parameters of the tube-side feed, furnace-side feed and combustion chamber refractory walls are consistent with typical plant data (Latham, 2008).

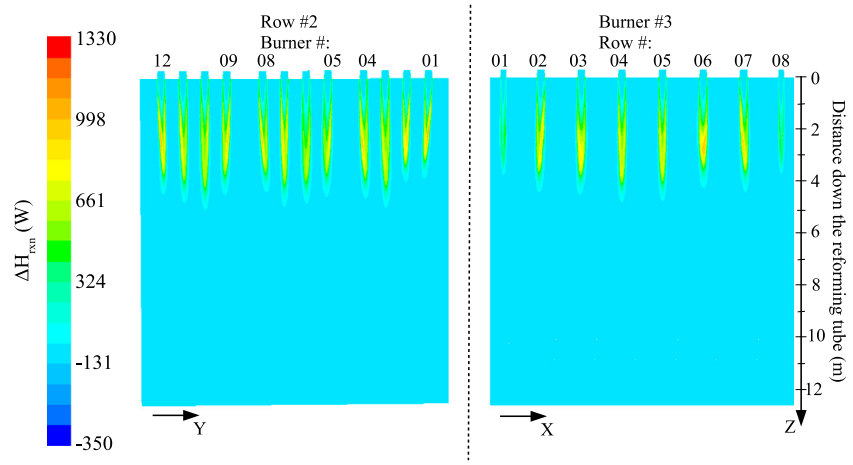

Fig. 8. Lateral (left) and frontal (right) contour maps of energy released by the furnace-side oxidation predicted by the reformer CFD simulation in which the parameters of the tube-side feed, furnace-side feed and combustion chamber refractory walls are consistent with typical plant data (Latham, 2008).

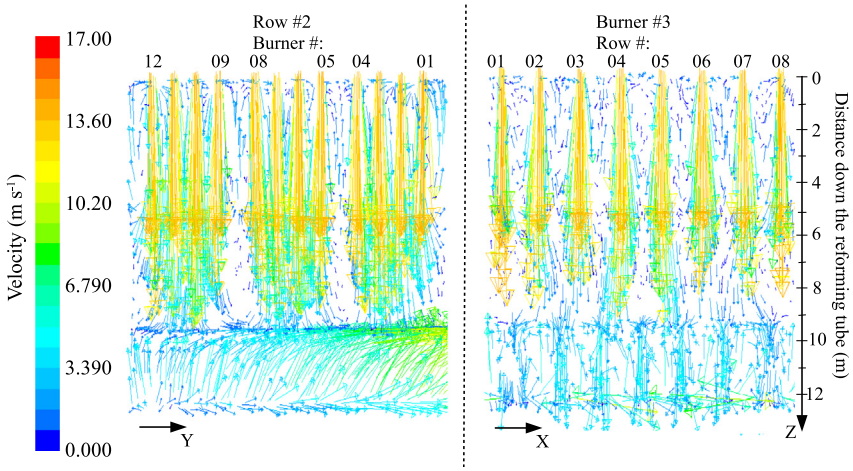

Fig. 9. Lateral (left) and frontal (right) contour maps of the furnace-side velocity magnitude predicted by the reformer CFD simulation in which the parameters of the tube-side feed, furnace-side feed and combustion chamber refractory walls are consistent with typical plant data (Latham, 2008).

top-fired reformers can be seen in the presented solution of the reformer CFD model. Particularly, Figs. 7 and 16 indicate that the maximum furnace-side temperature is located in the upper part of the reformer (de Lasa et al., 1992; Latham et al., 2011), and Fig. 8 demonstrates that the flame length is consistent with the typical values between ~4.5 m and ~6 m (Latham, 2008).

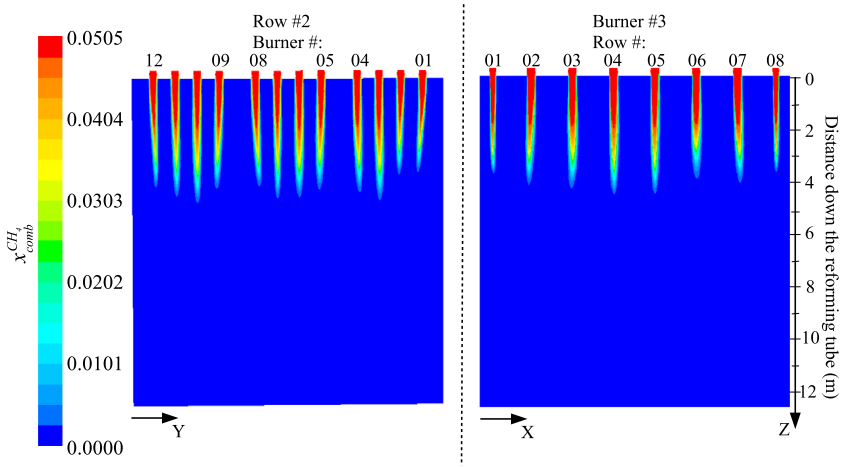

Fig. 10. Lateral (left) and frontal (right) methane mole fraction contour maps inside the combustion chamber predicted by the reformer CFD simulation in which the parameters of the tube-side feed, furnace-side feed and combustion chamber refractory walls are consistent with typical plant data (Latham, 2008).

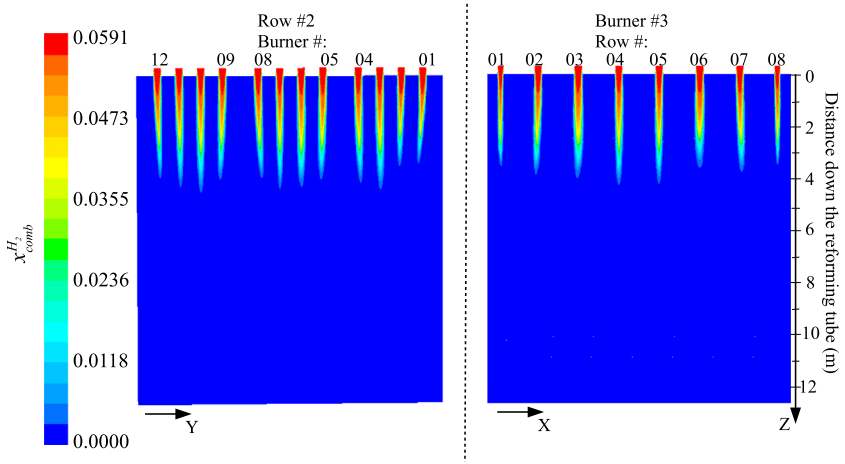

Fig. 11. Lateral (left) and frontal (right) hydrogen mole fraction contour maps inside the combustion chamber predicted by the reformer CFD simulation in which the parameters of the tube-side feed, furnace-side feed and combustion chamber refractory walls are consistent with typical plant data (Latham, 2008).

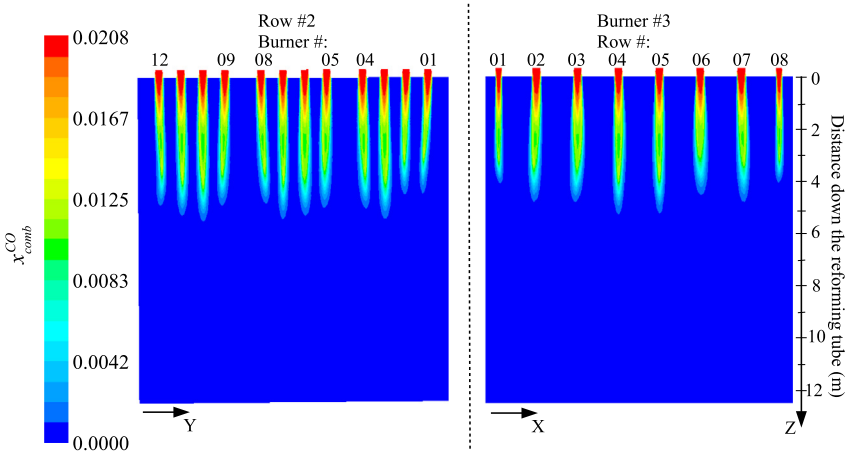

Fig. 12. Lateral (left) and frontal (right) carbon monoxide mole fraction contour maps inside the combustion chamber predicted by the reformer CFD simulation in which the parameters of the tube-side feed, furnace-side feed and combustion chamber refractory walls are consistent with typical plant data (Latham, 2008).

Furthermore, the simulation data of the reformer CFD model indicates that approximately 55.1% of the thermal energy released by this process is transferred to the reforming tubes, 3% of which dissipates to the surrounding air through the chamber refractory walls and the remainder of which exits the reformer at the combustion chamber outlets, which is in close agreement with typical

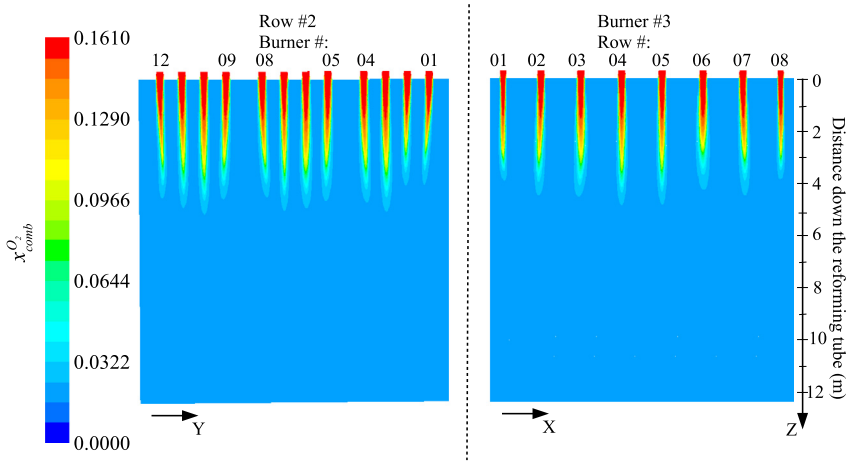

Fig. 13. Lateral (left) and frontal (right) oxygen mole fraction contour maps inside the combustion chamber predicted by the reformer CFD simulation in which the parameters of the tube-side feed, furnace-side feed and combustion chamber refractory walls are consistent with typical plant data (Latham, 2008).

plant data (Latham, 2008; de Lasa et al., 1992). Finally, the solution of the reformer CFD model suggests that the SMR process is near equilibrium at the reforming tube outlets as expected. Specifically, Fig. 15 shows that the slopes of the composition profiles, which are

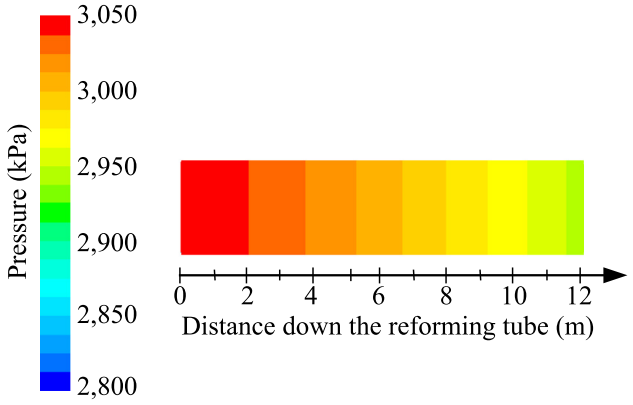

Fig. 14. Tube-side pressure contour map predicted by the reformer CFD simulation in which the parameters of the tube-side feed, furnace-side feed and combustion chamber refractory walls are consistent with typical plant data (Latham, 2008).

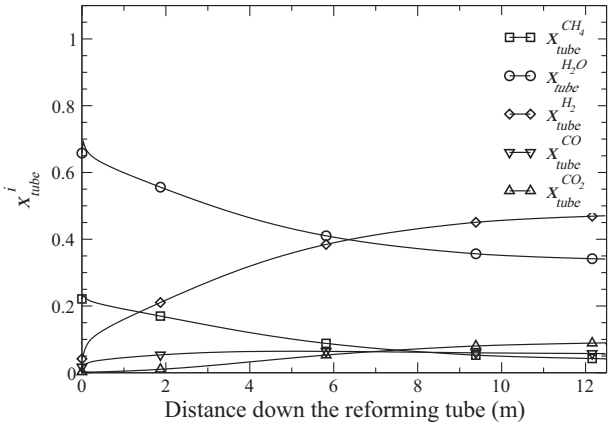

Fig. 15. Radial-weighted average tube-side compositions predicted by the reformer CFD simulation in which the parameters of the tube-side feed, furnace-side feed and combustion chamber refractory walls are consistent with typical plant data (Latham, 2008).

indicative of the net reaction rates of the tube-side species at the reforming tube outlet, are close to zero.

We next compare our numerical results with those from typical plant data. When typical plant data is employed to justify the validity of the simulation results produced by the reformer CFD model, the data needs to be normalized to unity as follows:

$$\bar{z}^{*} = \frac{\bar{z} - \bar{z}_{min}}{\bar{z}_{max} - \bar{z}_{min}} \tag{13}$$

where $\bar{z}$ and $\bar{z}^{*}$ are the original data and corresponding normalized data, respectively, and $\bar{z}_{max}$ and $\bar{z}_{min}$ are the maximum and minimum values of the data set of interest. This is because many variations of top-fired reformer geometries are employed in the previous experimental and computational works of the SMR process, and the typical plant data are commonly reported in deviation forms for proprietary reasons. Figs. 17 and 18 compare the normalized CFD data with the normalized typical plant data presented in Latham (2008) and Latham et al. (2011). It is noted that we refer to the data from Latham (2008) and Latham et al. (2011) as typical plant data though it is generated from a first-principles reformer model in which the combustion of the furnace-side feed was not simulated simultaneously with the reforming tubes, and a predefined heat

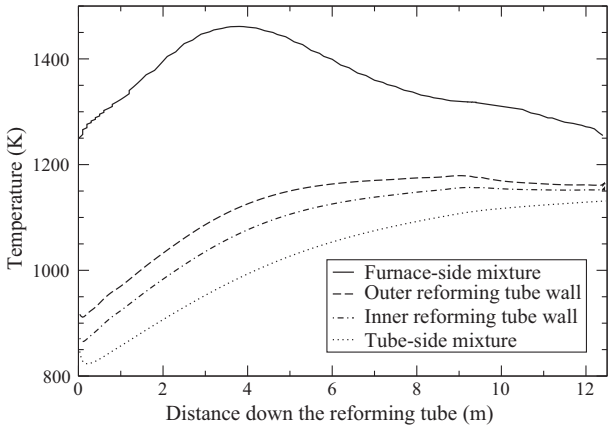

Fig. 16. Average temperature profiles of the furnace-side mixture (solid line), outer reforming tube wall (dashed line), inner reforming tube wall (dash-dotted line) and tube-side mixture (dotted line) predicted by the reformer CFD simulation in which the parameters of the tube-side feed, furnace-side feed and combustion chamber refractory walls are consistent with typical plant data (Latham, 2008).

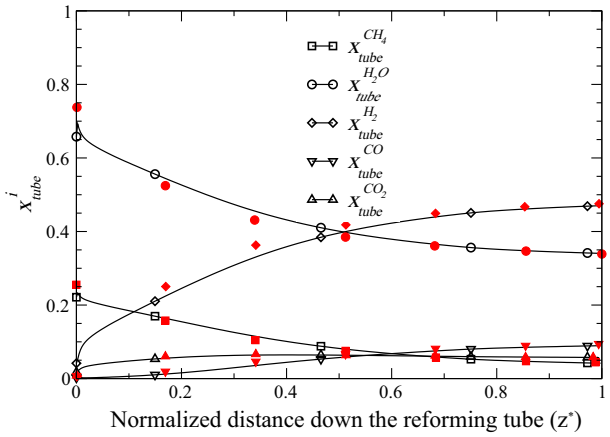

Fig. 17. Radial-weighted average tube-side compositions along the reforming tubes produced by the reformer CFD model (black) versus those derived from typical plant data of the SMR process (red) (Latham, 2008). (For interpretation of the references to colour in this figure legend, the reader is referred to the web version of this article.)

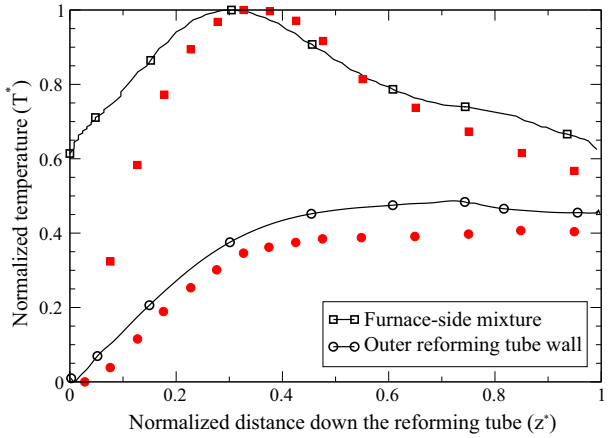

Fig. 18. Average temperature profiles of the furnace-side mixture and outer reforming tube wall produced by the reformer CFD model (black) versus those derived from typical plant data of the SMR process (red) (Latham et al., 2011). (For interpretation of the references to colour in this figure legend, the reader is referred to the web version of this article.)

released profile was used. In addition, the reforming tube models from those works are modeled by the 1-D plug flow reactor model and thus ignore the radial spatial gradients of transport variables and the effect of the flow pattern on the reforming tubes. Nevertheless, the models from Latham (2008) and Latham et al. (2011) employ a number of adjustable empirical constants (e.g., the heat-release length, the predefined parabolic heat-release profile, the gray gas model, and the convective heat transfer coefficients) that are tuned so that the estimated temperature profile of the outer reforming tube wall is consistent with the experimental data recorded by the high-cost monitoring IR cameras of an on-line reformer. Thus, we consider that the data from these works can be considered to be sufficiently close to experimental plant data to be utilized in validating the reformer CFD model. Therefore, the data from Latham (2008) and Latham et al. (2011) is used to validate the proposed modeling strategies that lead to the development of the reformer CFD model from Sections 4–7. Specifically, Fig. 17 shows that the composition profiles of the tube-side species along the reforming tube length vary in a manner that is consistent with the previous work, which justifies the choice of the global kinetic model of the SMR process with the universal effectiveness factor and the FR/ED model for accounting for turbulence-chemistry interaction. Additionally, Fig. 18 demonstrates that the average temperature profiles of the furnace-side mixture and outer reforming tube wall along the length of the reforming tube closely resemble the corresponding profiles reported in the previous reformer study, which validates the choice of the radiative property correlation and heat transfer model, as well as the neglect of radiation in the tube side and the use of the porous zone function for modifying the heat transfer equations in the reforming tubes. Specifically, the outer reforming tube wall temperatures from the reformer CFD model and Latham et al. (2011) are similar, and the temperature profiles for the furnace-side mixture have a similar shape in the sense that both demonstrate a maximum furnace-side temperature that is located in the upper part of the reformer (i.e., a characteristic of top-fired reformers). Differences between the furnace-side mixture temperature profiles of the CFD simulation and Latham et al. (2011) are expected since in Latham et al. (2011), the effects of the furnace-side flow pattern on the temperature of the furnace-side mixture are ignored as the combustion chamber is assumed to behave like a plug flow reactor. As additional validation of the reformer CFD simulation results, the values of a number of properties of the tube-side mixture from Latham (2008) are compared with those from the reformer CFD model in Table 6 and show good agreement.

The converged reformer CFD solution is validated by the CFD data generated by the industrial-scale reforming tube CFD model developed in Lao et al. (2016). The industrial-scale reforming tube CFD model is updated with the same modeling parameters as described in Sections 2, 5 and 6, and implemented with the tube-side feed conditions and outer reforming tube wall profile (Fig. 16) of the reformer CFD model. Table 6 indicates that the differences between the CFD data generated by the reformer CFD model and updated industrial-scale reforming tube CFD model are not significant.

Furthermore, the converged reformer CFD solution is validated by the data generated by a standard reforming Gibbs reactor model of a steady-state process simulator (e.g., Pro/II) as shown in Table 6. Because the tube-side reactions have been demonstrated above through Fig. 15 to have approximately reached equilibrium at the reactor outlet, it is expected that the mole fractions at the tube outlet from the CFD simulation would correspond with the results from the Gibbs reactor simulation. The reforming Gibbs reactor model is provided with the Gibbs reactor feed stream and duty, which are set to the tube-side feed and the average thermal energy absorbed by each reforming tube of 345.090 kW derived from the reformer CFD solution, respectively. The differences in the results between the reformer CFD model and the reforming Gibbs reactor model are demonstrated in Table 6 to be small. It is important to note that the solution of the reforming Gibbs reactor model can only be obtained after the solution of the reformer CFD model has already been computed from which the total energy absorbed by each reforming tube is extracted. One might suggest that the total energy absorbed by each reforming tube can be back-calculated given the tube-side composition at the reforming tube outlets; however, prior to the completion of the reformer CFD simulation, neither the amount of thermal energy absorbed by the reforming tubes (i.e., the energy uptake of a reforming Gibbs reactor model) nor the tube-side composition at the reforming tube outlets (i.e., the approximated yield of the SMR process) are available to be used as inputs. Hence, it is evident that the reforming Gibbs reactor model is not designed to replace the reformer CFD model, and more details are given in Remark 4.

Next, the area-weighted average heat flux across the reforming tube wall predicted by the reformer CFD model is compared to that of the typical plant data reported in the literature as shown in

Table 7
Validation of reformer CFD model by available plant data from literature.

	Average heat flux (kW m^{-2})
Reformer CFD model	70
Lao et al., (2016)	71
Latham (2008)	67
Rostrup-Nielsen (1984)	45–90
Dybkjaer (1995)	79
Froment and Bischoff (1990)	76
Pantoleontos et al. (2012)	<80

Table 7. The average heat flux in Table 7 from Latham (2008) is estimated based on the outer and inner reforming tube wall temperature profiles reported in that work, the reforming tube thermal conductivity of $106,500\ \mathrm{J\ m^{-1}\ h^{-1}\ K^{-1}}$ and the typical reforming tube wall thickness of 0.015 m. From Table 7, the area-weighted average heat flux across the reforming tube wall predicted by the reformer CFD model is consistent with that of the typical plant data.

Finally, the reformer CFD model is implemented with the furnace-side feed distribution of an on-line reformer provided by a third party, and the corresponding converged CFD data is obtained by the proposed step-by-step convergence strategy as discussed in Section 8. Subsequently, the CFD data is compared with the recorded plant data, which is an outer reforming tube wall temperature distribution at a fixed axial location (as shown in Fig. 19) and is collected by a system of IR cameras situated around the reformer as discussed in Section 4.2. The outer reforming tube wall temperature distribution constructed based on the CFD simulation and information of the approximate views of the IR cameras is consistent with the plant data provided by the third party as the maximum deviation at any location is ~3% and the average deviation is ~1.2% as shown in Fig. 20. The blank spaces shown in Fig. 20 represent reforming tubes for which no temperature measurements were provided from the reported data. However, from the good agreement of our CFD data with the available data, the CFD results for these additional reforming tubes are expected to be indicative of the actual operating conditions. This highlights the utility of CFD modeling for obtaining information regarding operating conditions that are perhaps not available from standard process monitoring techniques (e.g., the outer wall temperature at all z locations down the reforming tube length, for every reforming tube) which may be required for assessing whether potentially dangerous operating conditions exist (e.g., any reforming tube outer wall temperature exceeding the maximum operating temperature at any z location) and modifying the process inputs to ameliorate such conditions when they are detected.

Based on the above, the simulation results produced by the reformer CFD model are demonstrated to be consistent with phenomena observed in reformers and to be in close agreement with the typical plant data. As a result, the converged solution of the reformer CFD model can be considered to be a reasonably reliable representation of experimental data and can be utilized to characterize the velocity, turbulence, composition and temperature fields inside the reformer.

Remark 2. In this work, we focus on presenting only modeling strategies that are expected to be most suitable for modeling the expected transport and reaction phenomena among the choices offered by ANSYS Fluent for the purpose of demonstrating how a high-fidelity CFD model of a reformer can be devised. Showing how initial modeling strategies can be selected for reasonably accurate results within a reasonable time frame is a significant contribution of the present work, because the coupling between the various transport and reaction phenomena in and between the tube and

Table 8
Notations.

A_{comb}	Total surface area of the combustion chamber (m^2)
C_p	Specific heat capacity of the furnace-side mixture (J kg^{-1} K^{-1})
$C^j_{p,comb}$	Heat capacity of species j in the furnace-side mixture (J kg^{-1} K^{-1})
D_p	Effective diameter of the catalyst pellets (m)
$D^{m,i}_{comb}$	Mass diffusion coefficient of the species i in the furnace-side mixture (m^2 s^{-1})
$D^{m,t}_{comb}$	Turbulent mass diffusion coefficient of the furnace-side mixture (m^2 s^{-1})
E_{comb}	Specific internal energy of the furnace-side mixture (J kg^{-1})
E_{wave}	Energy of electromagnetic waves (J)
P_{comb}	Pressure of the furnace-side mixture (kPa)
p^i_{tube}	Partial pressure of the species i in the tube-side mixture (bar)
$\vec{g}$	Universal gravitational acceleration vector (m s^{-2})
h	Plank's constant
h_{comb}	Specific sensible enthalpy of the furnace-side mixture (J kg^{-1})
h^j_{comb}	Specific sensible enthalpy of species j in the furnace-side mixture (J kg^{-1})
K_{H_2}	Adsorption constant for H_2 (bar^{-1})
K_{CH_4}	Adsorption constant for CH_4 (bar^{-1})
K_{CO}	Adsorption constant for CO (bar^{-1})
K_{H_2O}	Dissociative constant for H_2O
K_1	Equilibrium constant of reaction 5 (bar^2)
K_2	Equilibrium constant of reaction 6
K_3	Equilibrium constant of reaction 7 (bar^2)
k_1	Forward kinetic constant coefficient of reaction 5 (kmol bar$^{1/2}$ (kg of catalyst)$^{-1}$ h^{-1})
k_2	Forward kinetic constant coefficient of reaction 6 (kmol (kg of catalyst)$^{-1}$ h^{-1} bar^{-1})
k_3	Forward kinetic constant coefficient of reaction 7 (kmol bar$^{1/2}$ (kg of catalyst)$^{-1}$ h^{-1})
k^{eff}_{comb}	Effective thermal conductivity of the furnace-side mixture (W m^{-1} K^{-1})
k^l_{comb}	Thermal conductivity of the furnace-side mixture (W m^{-1} K^{-1})
k^t_{comb}	Turbulent thermal conductivity of the furnace-side mixture (W m^{-1} K^{-1})
k_{comb}	Turbulence kinetic energy of the furnace-side mixture (m^2 s^{-2})
I	Unit tensor
$\vec{J}^i_{comb}$	Turbulent mass diffusion flux of species i of the furnace-side mixture (kg m^{-2} s^{-1})
$R_i, i = 1,\ldots,4$	Intrinsic volumetric reaction rate of the ith reaction (kmol m^{-3} s^{-1})
$R_i, i = 5,\ldots,7$	Intrinsic volumetric reaction rate of the ith reaction (kmol (kg of catalyst)$^{-1}$ s^{-1})
$R_{i,j}$	Observed volumetric rate of species i in reaction j (kg m^{-3} s^{-1})
M_i	Molecular weight of species i (kg kmol^{-1})
$M_{\mathcal{R}}$	Molecular weight of a specified reactant $\mathcal{R}$ (kg kmol^{-1})
L	Characteristic dimension of the combustion chamber (m)
L_{tube}	Heated reforming tube length (m)
Sc^t_{comb}	Turbulent Schmidt number of the furnace-side mixture
T_{comb}	Temperature of the furnace-side mixture (K)
T_{ref}	Reference temperature (K)
$[i]$	Molar concentration of the species i of the furnace-side mixture (kmol m^{-3})
x^i_{tube}	Mole fraction of species i in the tube-side mixture
x^i_{comb}	Mole fraction of species i in the furnace-side mixture
Y_i	Mass fraction of species i
Y^i_{comb}	Mass fraction of species i in the furnace-side mixture
$Y_{\mathcal{R}}$	Mass fraction of a specified reactant $\mathcal{R}$ in reaction j
$Y_{\mathcal{P}}$	Mass fraction of a specified product species $\mathcal{P}$ in reaction j
V_{comb}	Volume of the combustion chamber (m^3)
$v_{\infty,tube}$	Superficial velocity of the tube-side mixture (m s^{-1})
$\vec{v}_{comb}$	Mass-averaged velocity vector of the furnace-side mixture (m s^{-1})
$v^2_{comb}/2$	Specific kinetic energy of the furnace-side mixture (J kg^{-1})
α	Permeability coefficient of the catalyst network (m^2)
β	Inertial resistance coefficient of the catalyst network (m^{-1})

(*continued on next page*)

Table 8 (*continued*)

β'	Coefficient of thermal expansion of the furnace-side mixture (K^{-1})
$\nu_{i,j}$	Stoichiometric coefficient of species i in reaction j
$\nu_{\Re,j}$	Stoichiometric coefficient of a specified reactant $\Re$ in reaction j
ν_{wave}	Frequency of electromagnetic waves (s^{-1})
ρ_{tube}	Density of the tube-side mixture (kg m^{-3})
ρ_{comb}	Density of the furnace-side mixture (kg m^{-3})
ϵ_{rad}	Total emissivity of the furnace-side mixture
ϵ_{comb}	Dissipation rate of the furnace-side mixture (m^2 s^{-3})
σ_a	Absorption coefficient of the furnace-side mixture
$\overline{\overline{\tau}}_{comb}$	Stress tensor (kPa)
γ	Porosity of the catalyst network
μ_{comb}	Molecular viscosity of the furnace-side mixture (kg m^{-1} s^{-1})
μ^t_{comb}	Eddy viscosity of the furnace-side mixture (kg m^{-1} s^{-1})
μ_{tube}	Molecular viscosity of the tube-side mixture (kg m^{-1} s^{-1})
$-\nabla \cdot \vec{q}_{rad}$	Radiative heat transfer rate (J m^{-3} s^{-1})
ΔP_{tube}	Pressure difference of the tube-side mixture across the catalyst network (kPa)

furnace sides prevents CFD results of the reformer from being generated for comparison with typical plant data until all phenomena have been included within the CFD simulation. Therefore, we focus only on the selection of initial modeling strategies that allow CFD data to be obtained that shows good agreement with typical plant data. Fine-tuning of the models for various phenomena (e.g., re-running the CFD simulation with alternative models such as alternative turbulence-chemistry interaction models to analyze whether this improves the agreement of the CFD results with typical plant data) could be performed, particularly by industry with significant plant data that can be used for distinguishing between the differences in accuracy at this fine-tuning step, but given the already significant agreement with typical plant data, changing the modeling strategies chosen would not conceptually change the novelty of the work (developing a step-by-step guide for obtaining a high-fidelity CFD model of an industrial-scale reformer), and thus is not pursued. The good agreement of the typical plant data with our CFD simulation results indicates that all simplifications and assumptions made in the development of the reformer CFD modeling strategies and meshing as described in Sections 2–7 were sufficient for obtaining a CFD model that can be considered to be a reasonable substitute for experimental data.

Remark 3. In this work, we assume that the furnace-side feed is uniformly distributed among all inner-lane burners and among all outer-lane burners, which results in symmetry in the furnace-side feed distribution and geometry that could have been exploited for the simulation. However, the intended application of the reformer CFD model is for allowing the evaluation of reformer operating parameters to improve the economics of operation when such operating changes cannot be fully evaluated any other way (for example, furnace balancing, which is optimizing the furnace-side feed distribution so that the temperature distribution of the outer reforming tube wall at a given length down the reforming tubes becomes more uniform). Evaluating the most optimal operating conditions may require the flexibility of simulating asymmetry within the reactor (e.g., an asymmetrical furnace-side feed distribution). Furthermore, the furnace-side feed flow rate to each burner is controlled by the percent opening of the corresponding valve, and therefore, valve-related disturbances (e.g., the valve stickiness) can cause an unintended asymmetric furnace-side feed distribution. For such reasons, it is beneficial to simulate the entire reformer, without exploiting symmetry, in the development of the reformer CFD model.

Remark 4. The comparison of the Gibbs reactor simulation results and those from the outlet of a reforming tube in the reformer CFD model in Table 6 does not indicate that steady-state simulations that are standard in the chemical process industries can serve as substitutes for a CFD model of a reformer. The CFD simulations reveal details about the reactor operation (e.g., the flame length, maximum and minimum temperatures of the reforming tube walls at any given axial location in the reformer, and the effect of changes in the burner feed flow rates on these maximum and minimum temperatures) that cannot be obtained from steady-state simulations such as a Gibbs reactor, and cannot even be obtained from standard experimental measurements that are taken from an on-line reformer (e.g., temperatures of specific reforming tube walls at specific axial locations determined from infrared cameras). It is also notable that due to the effects of the geometry on the flows and heat transfer within the reformer (for example, asymmetry in the flow field within the furnace side is observed in Fig. 9 due to the flue gas tunnel exits being located on only one side of the reformer, which creates non-identical environments for the reforming tubes throughout the reformer despite the fact that they

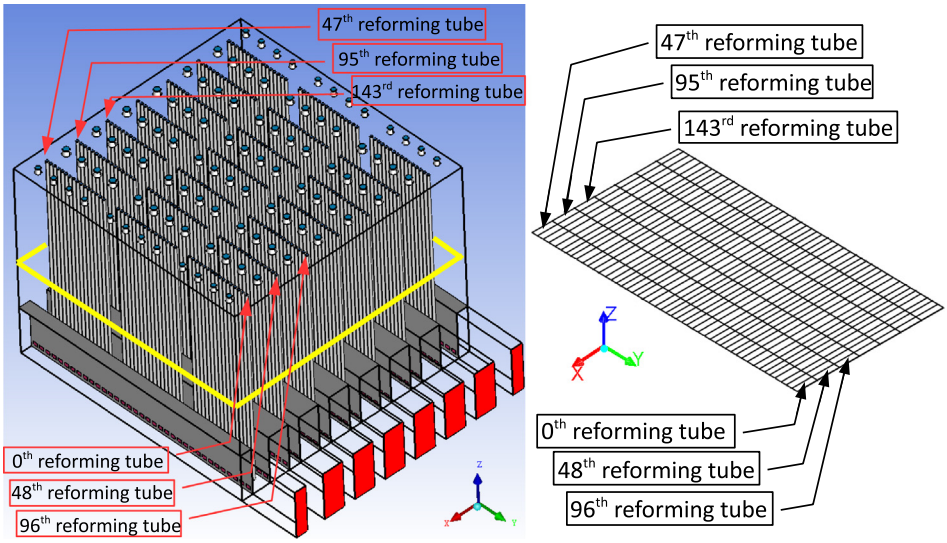

Fig. 19. Description of the layout of the outer reforming tube wall temperature distribution, in which each grid contains an average outer reforming tube wall temperature of the corresponding reforming tube recorded by a system of IR cameras situated around the reformer.

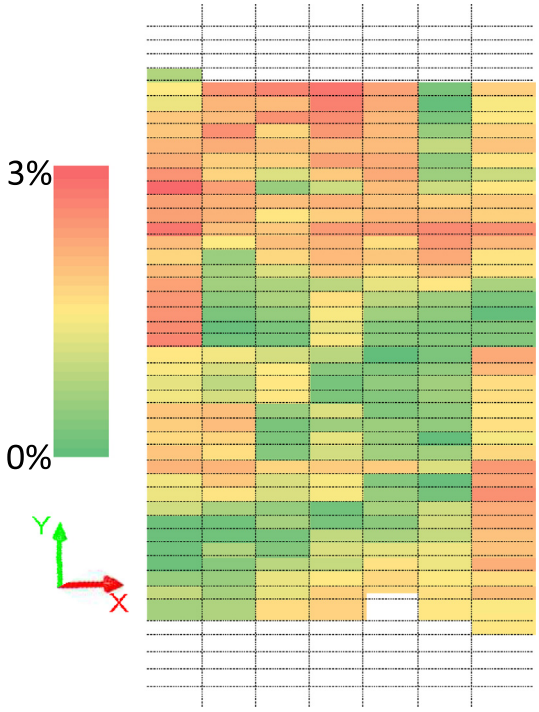

Fig. 20. Distribution of the percent difference in the outer reforming tube wall temperature between the reformer CFD data and the plant data provided by the third party. The percent difference of each reforming tube is computed by the ratio of the deviation of the CFD data from the corresponding plant data to the corresponding plant data.

are fed with identical feeds), as well as the interactions of the flow and heat transfer with the observed reaction rates, our prior works (Lao et al., 2016; Aguirre et al., 2017) cannot predict the effects seen in a reformer as the present work can because they utilize different geometries and modeling strategies. Therefore, the novelty of the present work hinges on the fact that because it demonstrates how a reformer CFD model can be developed and validated (i.e., it develops neither a simplified model like a Gibbs reactor nor even a smaller-scale CFD model), it demonstrates a methodology for obtaining high-fidelity data regarding the operating conditions throughout a reformer that can be considered to be representative of the actual conditions within the reformer but cannot be obtained any other way. The development of such a model is significant therefore for industry, because it provides a methodology for optimizing process operation with highly reliable data that is not otherwise available and allows problematic operating conditions to be evaluated and mitigated. Furthermore, the discussion of why the CFD modeling strategies were chosen demonstrates how expected phenomena within a reactor can be evaluated to allow for appropriate modeling strategies to be chosen for CFD simulation of other reactors of industrial interest for which such high-fidelity data would be beneficial.

11. Conclusion

The present work detailed the development of a CFD model of a steam methane reformer and presented a methodology for analyzing expected transport and reaction phenomena to choose modeling strategies within the CFD software that result in CFD simulation data that can be considered to be a substitute for experimental data. The reformer model simulates the essential transport phenomena observed in industrial high-temperature applications as well as reformer-relevant physical and chemical phenomena. Specifically, the standard $k-\epsilon$ turbulence model, FR/ED model and global kinetic models of hydrogen/methane combustion were selected to simulate the non-premixed combustion characteristics, the reaction rates of the furnace-side species and the thermal energy released from the oxidation of the furnace-side feed under the influence of turbulence. Then, a correlation between the furnace-side radiative properties and temperature, Kirchhoff's law, Lambert Beer's law and the discrete ordinate method were chosen to simulate radiative heat transfer within the furnace-side mixture and between the furnace-side mixture and solid surfaces inside the reformer. Next, the standard $k-\epsilon$ turbulence model, FR/ED model and global kinetic model of the SMR process were utilized to simulate the reaction rates of the tube-side species under the influence of turbulence. Lastly, the modeling strategy of the reforming tubes utilized an approximate representation of the catalyst network to simulate the presence of catalyst particles inside the reforming tube and the effect of internal and external diffusion limitations on the observed reaction rates of the tube-side species. We recognize that the computing time required to complete a simulation of the reformer CFD model by ANSYS Fluent on 80 cores of UCLA's Hoffman2 cluster is significant (i.e., approximately three full days), yet the upfront investment (i.e., time) makes it possible for us to determine the optimized operating conditions of the reformer. Specifically, the simulation results generated by the reformer CFD model with the tube-side and furnace-side feeds derived from typical plant data are demonstrated to be consistent with phenomena observed in reformers and to be in close agreement with typical plant data. In addition, the simulation data generated by the reformer CFD model, in which the tube-side and furnace-side feed distributions provided by a third party are used as boundary conditions, is shown to be in close agreement with the plant data recorded from the on-line reformer at the hydrogen manufacturing plant. Therefore, the reformer CFD model can be considered to be an adequate representation of the on-line reformer and can be used to determine the risk to operate the on-line reformer at un-explored and potentially more beneficial operating conditions.

Acknowledgements

Financial support from the Department of Energy is gratefully acknowledged.

References

Aguirre, A., Tran, A., Lao, L., Durand, H., Crose, M., Christofides, P.D., 2017. CFD modeling of a pilot-scale steam methane reforming furnace. In: Advances in Energy Systems Engineering. Springer, pp. 75–117.
Amirshaghaghi, H., Zamaniyan, A., Ebrahimi, H., Zarkesh, M., 2010. Numerical simulation of methane partial oxidation in the burner and combustion chamber of autothermal reformer. Appl. Math. Model. 34, 2312–2322.
ANSYS Inc., Nov. 2013. ANSYS Fluent Theory Guide 15.0.
Bane, S.P.M., Ziegler, J.L., Shepherd, J.E., 2010. Development of One-Step Chemistry Models for Flame and Ignition Simulations. Technical Report, GALCIT Report GALCITFM:2010.002.
Batdorf, M., Freitag, L.A., Ollivier-Gooch, C., 1997. Computational study of the effect of unstructured mesh quality on solution efficiency. In: Proceedings of the 13th AIAA Computational Fluid Dynamics Conference, Snowmass, CO.
Duan, R., Liu, W., Xu, L., Huang, Y., Shen, X., Lin, C.H., Liu, J., Chen, Q., Sasanapuri, B., 2015. Mesh type and number for the CFD simulations of air distribution in an aircraft cabin. Numer. Heat Transfer Part B: Fundam. 67, 489–506.
Dybkjaer, I., 1995. Tubular reforming and autothermal reforming of natural gas – an overview of available processes. Fuel Process. Technol. 42, 85–107.
Ergun, S., Orning, A.A., 1949. Fluid flow through randomly packed columns and fluidized beds. Indust. Eng. Chem. 41, 1179–1184.
Ewan, B., Allen, R., 2005. A figure of merit assessment of the routes to hydrogen. Int. J. Hydrogen Energy 30, 809–819.
Froment, G.F., Bischoff, K.B., 1990. Chemical Reactor Analysis and Design. Wiley, New York.
Jones, W.P., Launder, B.E., 1972. The prediction of laminarization with a two-equation model of turbulence. Int. J. Heat Mass Transfer 15, 301–314.

Kroschwitz, J.I., Howe-Grant, M. (Eds.), 1999. Kirk-Othmer Encyclopedia of Chemical Technology. John Wiley and Sons, Inc., New York.
Kuroki, M., Ookawara, S., Ogawa, K., 2009. A high-fidelity CFD model of methane steam reforming in a packed bed reactor. J. Chem. Eng. Jpn. 42, S73–S78.
Lao, L., Aguirre, A., Tran, A., Wu, Z., Durand, H., Christofides, P.D., 2016. CFD modeling and control of a steam methane reforming reactor. Chem. Eng. Sci. 148, 78–92.
de Lasa, H.I., Dogŭ, G., Ravella, A. (Eds.), 1992. Chemical Reactor Technology for Environmentally Safe Reactors and Products. NATO ASI Series, vol. 225. Springer Science & Business Media, Dordrecht, The Netherlands.
Latham, D., 2008. Masters Thesis: Mathematical Modeling of an Industrial Steam Methane Reformer. Queen's University.
Latham, D.A., McAuley, K.B., Peppley, B.A., Raybold, T.M., 2011. Mathematical modeling of an industrial steam-methane reformer for on-line deployment. Fuel Process. Technol. 92, 1574–1586.
Launder, B.E., Sharma, B.I., 1974. Application of the energy dissipation model of turbulence to the calculation of flow near a spinning disc. Lett. Heat Mass Transfer 1, 131–137.
Lipman, T., 2011. An overview of hydrogen production and storage systems with renewable hydrogen case studies. Technical Report.
Luan, Y.T., Chyou, Y.P., Wang, T., 2013. Numerical analysis of gasification performance via finite-rate model in a cross-type two-stage gasifier. Int. J. Heat Mass Transfer 57, 558–566.
Magnussen, B.F., 2005. The eddy dissipation concept: a bridge between science and technology. In: ECCOMAS Thematic Conference on Computational Combustion, Lisbon, Portugal.
Magnussen, B.F., Hjertager, B.H., 1977. On mathematical modeling of turbulent combustion with special emphasis on soot formation and combustion. In: Symposium (International) on Combustion. Elsevier, pp. 719–729.
Maximov, A., 2012. Thesis for the Degree of Doctor of Science: Theoretical Analysis and Numerical Simulation of Spectral Radiative Properties of Combustion Gases in Oxy/air-fired Combustion Systems. Lappeenranta University of Technology.
McGreavy, C., Newmann, M.W., 1969. Development of a mathematical model of a steam methane reformer. In: Proceedings of the Conference on the Industrial Applications of Dynamic Modelling, Durham, NC.
Mishra, S.C., Prasad, M., 1998. Radiative heat transfer in participating media–a review. Sadhana 23, 213–232.
Mokheimer, E.M., Hussain, M.I., Ahmed, S., Habib, M.A., Al-Qutub, A.A., 2015. On the modeling of steam methane reforming. J. Energy Resour. Technol., 012001
Nicol, D.G., 1995. Ph. D. Thesis: A Chemical Kinetic and Numerical Study of NOx and Pollutant Formation in Low-emission Combustion. University of Washington.
Olivieri, A., Vegliò, F., 2008. Process simulation of natural gas steam reforming: fuel distribution optimisation in the furnace. Fuel Process. Technol. 89, 622–632.
Pantoleontos, G., Kikkinides, E.S., Georgiadis, M.C., 2012. A heterogeneous dynamic model for the simulation and optimisation of the steam methane reforming reactor. Int. J. Hydrogen Energy 37, 16346–16358.
Pedernera, M.N., Piña, J., Borio, D.O., Bucalá, V., 2003. Use of a heterogeneous two-dimensional model to improve the primary steam reformer performance. Chem. Eng. J. 94, 29–40.
Rostrup-Nielsen, J.R., 1984. Catalysis: Science and Technology. Springer-Verlag, Berlin, Germany.
Rostrup-Nielsen, J.R., Rostrup-Nielsen, T., 2002. Large-scale hydrogen production. Cattech 6, 150–159.
Sadooghi, P., Rauch, R., 2013. Pseudo heterogeneous modeling of catalytic methane steam reforming process in a fixed bed reactor. J. Natural Gas Sci. Eng. 11, 46–51.
Seo, Y.S., Seo, D.J., Seo, Y.T., Yoon, W.L., 2006. Investigation of the characteristics of a compact steam reformer integrated with a water-gas shift reactor. J. Power Sources 161, 1208–1216.
Turns, S.R., 1996. An Introduction to Combustion: Concepts and Applications. McGraw-Hill, Boston, MA.
Udengaard, N.R., 2004. Hydrogen production by steam reforming of hydrocarbons. Preprint Papers-Am. Chem. Soc., Div. Fuel Chem. 49, 906–907.
Vuthaluru, R., Vuthaluru, H., 2006. Modelling of a wall fired furnace for different operating conditions using FLUENT. Fuel Process. Technol. 87, 633–639.
Wesenberg, M.H., Svendsen, H.F., 2007. Mass and heat transfer limitations in a heterogeneous model of a gas-heated steam reformer. Indust. Eng. Chem. Res. 46, 667–676.
Xu, J., Froment, G.F., 1989. Methane steam reforming, methanation and water-gas shift: I. Intrinsic kinetics. AIChE J. 35, 88–96.
Zamaniyan, A., Behroozsarand, A., Ebrahimi, H., 2010. Modeling and simulation of large scale hydrogen production. J. Natural Gas Sci. Eng. 2, 293–301.
Zamaniyan, A., Ebrahimi, H., Mohammadzadeh, J.S.S., 2008. A unified model for top fired methane steam reformers using three-dimensional zonal analysis. Chem. Eng. Process.: Process Intensif. 47, 946–956.
Zhang, J., Dai, B., Meng, Y., Wu, X., Zhang, J., Zhang, X., Ninomiya, Y., Zhang, Z., Zhang, L., 2015. Pilot-scale experimental and CFD modeling investigations of oxy-fuel combustion of Victorian brown coal. Fuel 144, 111–120.